The Astrophysical Journal, 917:15 (19pp), 2021 August 10 https://doi.org/10.3847/1538-4357/ac05c9

Observations and Analysis of CH^+ Vibrational Emissions from the Young, Carbon-rich Planetary Nebula NGC 7027: A Textbook Example of Chemical Pumping

David A. Neufeld[1], Benjamin Godard[2,3], P. Bryan Changala[4], Alexandre Faure[5], T. R. Geballe[6], Rolf Güsten[7], Karl M. Menten[7], and Helmut Wiesemeyer[7]
[1] Department of Physics & Astronomy, Johns Hopkins University, Baltimore, MD 21218, USA
[2] Observatoire de Paris, PSL Université, Sorbonne Université, LERMA, F-75014 Paris, France
[3] Laboratoire de Physique de l'Ecole normale supérieure, ENS, Université PSL, CNRS, Sorbonne Université, Université de Paris, F-75005 Paris, France
[4] Center for Astrophysics | Harvard & Smithsonian, Cambridge, MA 02138, USA
[5] Univ. Grenoble Alpes, CNRS, IPAG, F-38000 Grenoble, France
[6] Gemini Observatory and NSF/NOIRLab, 670 N. A'ohoku Place, Hilo, HI 96720, USA
[7] Max-Planck-Institut für Radioastronomie, Auf dem Hügel 69, D-53121 Bonn, Germany
Received 2021 March 23; revised 2021 May 20; accepted 2021 May 27; published 2021 August 10

Abstract

We discuss the detection of 14 rovibrational lines of CH^+, obtained toward the planetary nebula NGC 7027 with the iSHELL spectrograph on NASA's Infrared Telescope Facility (IRTF) on Maunakea. Our observations in the 3.49–4.13 μm spectral region, obtained with a 0.″375 slit width that provided a spectral resolving power $\lambda/\Delta\lambda \sim 80{,}000$, have resulted in the unequivocal detection of the $R(0)-R(3)$ and $P(1)-P(10)$ transitions within the $v=1-0$ band of CH^+. The R-branch transitions are anomalously weak relative to the P-branch transitions, a behavior that is explained accurately by rovibronic calculations of the transition dipole moment reported in a companion paper. Nine infrared transitions of H_2 were also detected in these observations, comprising the $S(8)$, $S(9)$, $S(13)$, and $S(15)$ pure rotational lines; the $v=1-0$ $O(4)-O(7)$ lines; and the $v=2-1$ $O(5)$ line. We present a photodissociation model, constrained by the CH^+ and H_2 line fluxes that we measured, that includes a detailed treatment of the excitation of CH^+ by inelastic collisions, optical pumping, and chemical ("formation") pumping. The latter process is found to dominate the excitation of the observed rovibrational lines of CH^+, and the model is remarkably successful in explaining both the absolute and relative strengths of the CH^+ and H_2 lines.

Unified Astronomy Thesaurus concepts: Planetary nebulae (1249); Interstellar molecules (849); Near infrared astronomy (1093); Interstellar line emission (844); Molecular spectroscopy (2095)

1. Introduction

Planetary nebulae present an unusual astrophysical environment in which a stratified shell of gas is irradiated by a central star with an effective temperature that may exceed 200,000 K. While the inner edge of such nebulae may be highly ionized and exhibit line emission from ions with appearance potentials in excess of 100 eV (e.g., Ne^{5+}), the gas temperature and degree of ionization drop with increasing distance from the star, and even molecular gas can exist within the outer parts of the shell. Molecules have been studied extensively in the young, carbon-rich planetary nebula NGC 7027, where roughly a dozen molecular species have been detected (e.g., Hasegawa & Kwok 2001; Zhang et al. 2008). These molecules have been observed primarily through their pure rotational emissions, although infrared rovibrational emissions from H_2 have been studied over several decades (e.g., Beckwith et al. 1980; Smith et al. 1981; Cox et al. 1997, 2002).

In the past year, rovibrational emissions from two additional molecules have been detected toward NGC 7027 (Neufeld et al. 2020, hereafter Paper I): HeH^+ and CH^+. Following the first astrophysical detection of HeH^+ by means of SOFIA/GREAT observations of its far-infrared $J=1-0$ pure rotational transition (Güsten et al. 2019), the $v=1-0$ $P(1)$ and $P(2)$ transitions of HeH^+ were detected in targeted observations using the iSHELL spectrometer on NASA's Infrared Telescope Facility (IRTF). These observations, which covered a substantial portion of the infrared L band, led to the serendipitous discovery of a series of emission lines, spaced nearly equally in fRequency, that were identified as the $v=1-0$ $R(0)-R(3)$ and $P(1)-P(5)$ transitions of CH^+. CH^+ is also a molecule that had previously been studied in NGC 7027 through far-infrared observations of its pure rotational lines (Cernicharo et al. 1997; Herpin et al. 2002; Wesson et al. 2010). Thus far, NGC 7027 is the only astrophysical source from which the infrared CH^+ rovibrational lines have been detected.

In this paper, we report the detection of four additional rovibrational emission lines of CH^+, obtained again by means of IRTF/iSHELL observations of NGC 7027; they are the $v=1-0$ $P(7)-P(10)$ transitions. The observations and data reduction are described in Section 2, and the results are presented in Section 3. In Section 4, we describe a comprehensive model for the formation, destruction, and excitation of CH^+ and compare its predictions with the observed CH^+ $v=1-0$ line fluxes. This model rests on new calculations, presented in a companion paper (Changala et al. 2021, hereafter C21), of the spontaneous radiative rates for CH^+ rovibrational transitions within the ground electronic state and for the $A^1\Pi - X^1\Sigma^+$ band. These calculations explain why the R-branch lines detected in the $v=1-0$ band of CH^+ are anomalously weak compared to the P-branch lines. In Section 5, we compare the model predictions with the observations. A brief summary follows in Section 6.

2. Observations and Data Reduction

The new observations of CH^+ reported here were performed at the IRTF on 2020 July 08 UT, using the iSHELL spectrograph (Rayner et al. 2016) in its `Lp3` grating setting

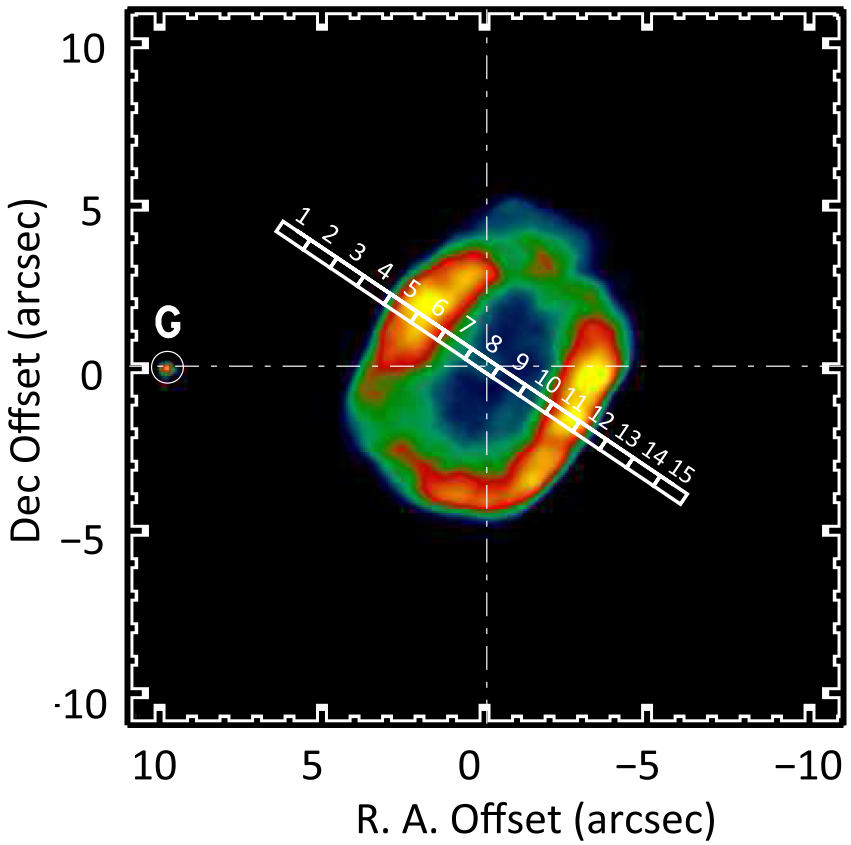

Figure 1. *K*-band image of NGC 7027, obtained with the slit viewing camera. White boxes indicate the aperture extraction regions adopted, with the numbering system used in the text. The R.A. and decl. offsets are given relative to the central star at $\alpha = 21^{\rm h}\,07^{\rm m}\,1\overset{\rm s}{.}793$, $\delta = 42^\circ\,14''\,9\overset{''}{.}79$ (J2000). "G" indicates the star used for guiding.

to cover the 3.817–4.155 μm spectral region.[8] The observing procedure was identical to that adopted for the previous observations and described in Paper I. Figure 1, reproduced from Paper I, shows the slit position on a *K*-band image of NGC 7027 that was obtained with the slit viewing camera and is dominated by emission from warm dust. The offsets shown here are relative to the position of the central star determined on the slit viewing camera: $\alpha = 21^{\rm h}07^{\rm m}1\overset{\rm s}{.}793$, $\delta = 42^\circ\,14''\,9\overset{''}{.}79$ (J2000).

The slit, of length 15″, was oriented at position angle 59° east of north. We selected a slit width of $0\overset{''}{.}375$, which provides a spectral resolving power $\lambda/\Delta\lambda \sim 80{,}000$. The $K = 11.3$ mag star 2MASS J21070267+4214099, marked with a "G" in Figure 1, was used as the guide star and kept on the same pixel of the detector throughout the integration. A reference position, located 16″ east of the center of the nebula, was used to record the blank-sky emission every 5 minutes while keeping the guide star inside the camera field of view.

The calibration procedures involved the acquisition of flat fields prior to every change in telescope pointing, the use of sky lines for wavelength calibration, and observations of the early-type (A0V) standard star HR 7001 (Vega) for flux calibration. The latter were performed at a similar air mass to that of NGC 7027 and were carried out with both the $0\overset{''}{.}375$- and $4\overset{''}{.}0$-wide slits in order that the slit-loss correction could be correctly determined for the unresolved standard star.

The data reduction methods were identical to those used for the 2019 data; full details are described in Paper I and will not be repeated here. The data reduction pipeline made use of the program suite *Spextool* ver. 5.0.2 (Cushing et al. 2004) adapted for the iSHELL data. This includes the *xtellcor* code (Vacca et al. 2003) for dividing the science spectra by the spectra of the standard star. The spectra were obtained for 15 extraction regions defined along the slit length (Figure 1), the size and the separation of which were each 1″. Using three stars in the field with Gaia astrometry, we determined (Paper I) that the extraction region number X (see Figure 1) is centered at an offset $\Delta\theta = X\ -8\overset{''}{.}1875$ from the central star. Here, the extraction regions are numbered 1 through 15 from NE to SW, with positive values of $\Delta\theta$ referring to offsets in the SW direction.

3. Results

3.1. Spectra, Position−Velocity Diagrams, and Line Fluxes

In this paper, we discuss the CH^+ emissions detected from NGC 7027 in the 3.265−4.155 μm spectral region covered by the `Lp1`, `Lp2`, and `Lp3` modes of iSHELL. In this bandpass, 14 rovibrational lines of CH^+ were detected unequivocally and are listed in Table 1, along with their wavelengths. This table

[8] These observations were followed by observations on 2020 July 11, 13, 14, and 15 with the `L2`, `L1`, `M1`, and `M2` settings, which—together with the `Lp1` and `Lp2` observations reported in Paper I—will provide a complete *L*- and *M*-band line survey of NGC 7027. Here, we focus on the `Lp1`, `Lp2`, and `Lp3` observations of CH^+ rovibrational emissions, while the full survey will be presented in a future paper.

Table 1
Spectral Lines of CH^+ Observed toward NGC 7027

Line	Rest Wavelength (μm)	Upper State Energy / k_B (K)	Peak Intensity in P–V Diagram[a] (MJy sr^{-1})	rms Noise (MJy sr^{-1})	Observed Line Flux[b] (10^{-18} W m^{-2})
CH^+ 1–0 $R(0)$	3.61463	3980	1125	102	2.35 ± 0.09
CH^+ 1–0 $R(1)$	3.58115	4058	1248	84	2.18 ± 0.06
CH^+ 1–0 $R(2)$	3.54960	4174	1107	69	1.47 ± 0.06
CH^+ 1–0 $R(3)$	3.51993	4328	770	71	1.09 ± 0.06
CH^+ 1–0 $R(4)$	3.49209	4520	267	86	0.21 ± 0.07
CH^+ 1–0 $R(8)$	3.39839	5667	225	102	-0.21 ± 0.09
CH^+ 1–0 $P(1)$	3.68758	3942	1885	211	3.97 ± 0.17
CH^+ 1–0 $P(2)$	3.72717	3980	3503	132	7.38 ± 0.11
CH^+ 1–0 $P(3)$	3.76891	4058	4615	134	8.33 ± 0.11
CH^+ 1–0 $P(4)$	3.81288	4174	4637	219	7.67 ± 0.15
CH^+ 1–0 $P(5)$	3.85914	4328	3709	85	7.21 ± 0.07
CH^+ 1–0 $P(6)$	3.90777	4520	N/A	N/A	6.45 ± 0.21
CH^+ 1–0 $P(7)$	3.95885	4751	3554	108	6.52 ± 0.08
CH^+ 1–0 $P(8)$	4.01249	5019	3633	122	5.04 ± 0.09
CH^+ 1–0 $P(9)$	4.06876	5324	3261	169	4.20 ± 0.13
CH^+ 1–0 $P(10)$	4.12777	5667	2955	253	3.46 ± 0.19

Notes.
[a] Maximum intensity when binned to 1″ with a 5 km s^{-1} channel width.
[b] In a 0.″375 × 15″ aperture.

Table 2
Spectral Lines of H_2 Observed toward NGC 7027

Line	Rest Wavelength (μm)	Upper State Energy / k_B (K)	Peak Intensity in P–V Diagram[a] (MJy sr^{-1})	rms Noise (MJy sr^{-1})	Observed Line Flux[b] (10^{-18} W m^{-2})
H_2 0–0 $S(8)$	5.05312	8677	4394	366	11.60 ± 0.23
H_2 0–0 $S(9)$	4.69461	10261	6739	228	19.04 ± 0.16
H_2 0–0 $S(13)$	3.84611	17444	1079	114	3.27 ± 0.10
H_2 0–0 $S(15)$	3.62617	21411	537	92	1.32 ± 0.08
H_2 1–0 $O(4)$	3.00387	6471	5980	151	23.91 ± 0.16
H_2 1–0 $O(5)$	3.23499	6951	10183	53	41.78 ± 0.05
H_2 1–0 $O(6)$	3.50081	7584	N/A	N/A	9.79 ± 0.17
H_2 1–0 $O(7)$	3.80742	8365	3962	129	11.70 ± 0.11
H_2 2–1 $O(5)$	3.43787	12550	765	114	2.09 ± 0.11

Notes.
[a] Maximum intensity when binned to 1″ with a 5 km s^{-1} channel width.
[b] In a 0.″375 × 15″ aperture.

includes two additional CH^+ transitions: the $v = 1-0$ $R(4)$ line, which is tentatively detected, and the $v = 1-0$ $R(8)$ line, for which we obtain an upper limit on the line flux. The intermediate $R(5)-R(7)$ lines fall at wavelengths that are inaccessible owing to atmospheric absorption. In addition, three rovibrational lines and two pure rotational lines of H_2 were detected in wavelength regions covered by the `Lp1`, `Lp2`, and `Lp3` modes of iSHELL, and two additional rovibrational lines and two pure rotational lines were detected using the `L2` and `M1` modes. The H_2 lines that we detected are listed in Table 2.

For CH^+, the line wavelengths are based on the spectroscopic parameters for $v = 0$ and $v = 1$ obtained by Hakalla et al. (2006) from measurements of the $A^1\Pi - X^1\Sigma^+$ band. Doménech et al. (2018) have reported direct (and more precise) wavelength measurements of four $v = 1-0$ transitions obtained by means of action spectroscopy, but such measurements have so far been limited to transitions involving upper states with rotational quantum numbers less than 3. We find that the Hakalla et al. (2006) spectroscopic parameters[9] yield a better fit to the set of astronomical data, which include lines with upper states of rotational quantum number as high as 9. For H_2, we adopt the line wavelengths presented recently by Roueff et al. (2019).

In Figures 2–4, we present position–velocity (P–V) diagrams for all the unequivocally detected lines in Tables 1 and 2, with the exception of the CH^+ $v = 1-0$ $P(6)$ and H_2 $v = 1-0$ $O(6)$ lines. These two lines are severely blended with

[9] The sextic distortion coefficients, H, obtained in the two studies show a discrepancy that is considerably larger than would be consistent with their stated uncertainties. The values and uncertainties given for H by Doménech et al. (2018) were based on a fit to the new wavelength determinations presented there in combination with previous measurements of the frequencies of pure rotational transitions (Yu et al. 2016); we find that the uncertainties given by Yu et al. (2016) for the latter measurements were likely underestimated, in agreement with conclusion reached by Cho & Le Roy (2016). We note also that the sextic distortion coefficients presented in Hakalla et al. (2006) are in much better agreement with theoretical estimates obtained by Sauer & Špirko (2013).

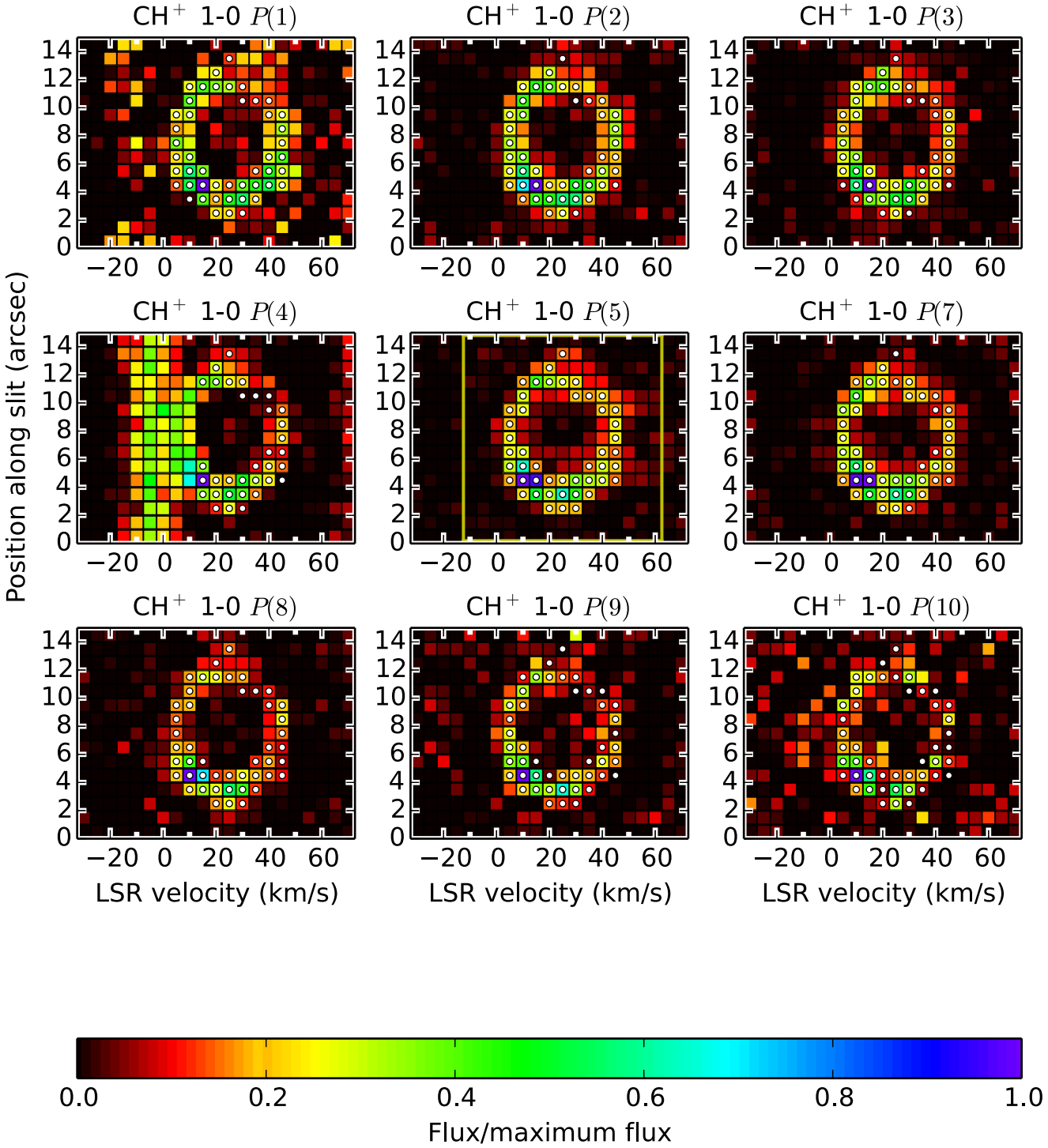

Figure 2. *P–V* diagrams for the CH^+ *P*-branch lines. The maximum intensities for each line are given in Table 1. Yellow rectangle: region used to determine the velocity-integrated flux for the $v = 1-0$ *P*(5) line. White circles: pixels used for flux determinations for other lines (with $v = 1-0$ *P*(5) as a template; see the text).

strong hydrogen recombination lines and required the special treatment discussed in Appendix A. In Figures 2–4, spatial position is represented along the vertical axis and Doppler shift along the horizontal. The former is the distance along the slit in arcseconds, binned to 1″, and the latter is the velocity relative to the local standard of rest (LSR), binned to 5 km s^{-1}. Each pixel is colored according to the intensity (color scale at bottom), normalized (separately for each transition) relative to the maximum flux in any pixel. The maximum intensities are listed in Tables 1 and 2. The *P–V* diagrams presented in Figures 2–4 show the intensities measured after subtraction of a zeroth-order continuum baseline at each position. In Figures 5 and 6, we show the continuum-subtracted spectra for all the unblended and equivocally detected lines listed in Tables 1 and 2, obtained from a sum over the full slit.

For all the lines shown in Figures 2–4, the *P–V* diagram shows a ring-like morphology, precisely the behavior expected when an expanding shell is observed using long-slit spectroscopy along the diameter. In the case of the strong CH^+ $v = 1-0$ *P*(5) line, we obtained an estimate of the total

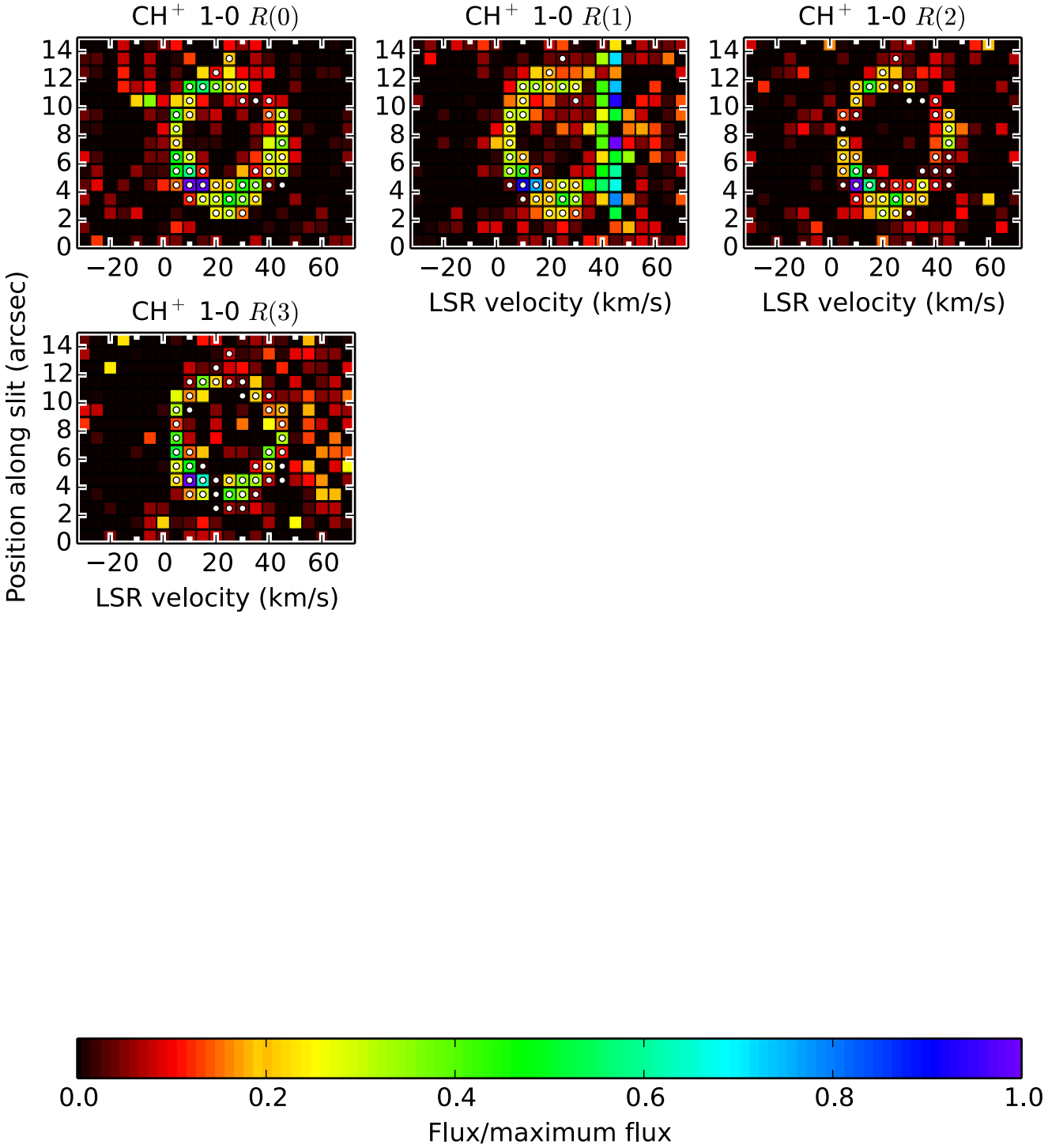

Figure 3. *P–V* diagrams for the CH^+ *R*-branch lines. The maximum intensities for each line are given in Table 1. White circles: pixels used for flux determinations (with $v = 1-0$ *P*(5) as a template; see the text).

velocity-integrated line flux by summing the flux measured within the yellow rectangle shown in the *P–V* diagram. This corresponds to an integration over LSR velocities ranging from -12.5 to $62.5\,\mathrm{km\,s^{-1}}$ and yields the value given in Table 1. Here, the line is detected at a signal-to-noise ratio of 60.

For weaker lines, however, the ring-like morphology in the *P–V* diagrams suggests that a more robust line detection strategy comes from considering the full two-dimensional data set prior to summing the spectra at different positions. For the CH^+ $v = 1-0$ *P*(5) line, the signal-to-noise ratio can be optimized if we include only the brightest *N* pixels within the yellow rectangle, where the optimal value of *N* is found to be 47. These pixels, marked with a white circle and representing 20% of all the pixels inside the yellow rectangle, define an annulus of strong emission for which the summed flux accounts for 80% of the total. For these pixels alone, the line is detected at a signal-to-noise ratio of 110.

To obtain the most robust determination of the fluxes for most other CH^+ lines in Table 1, therefore, we took a sum over the

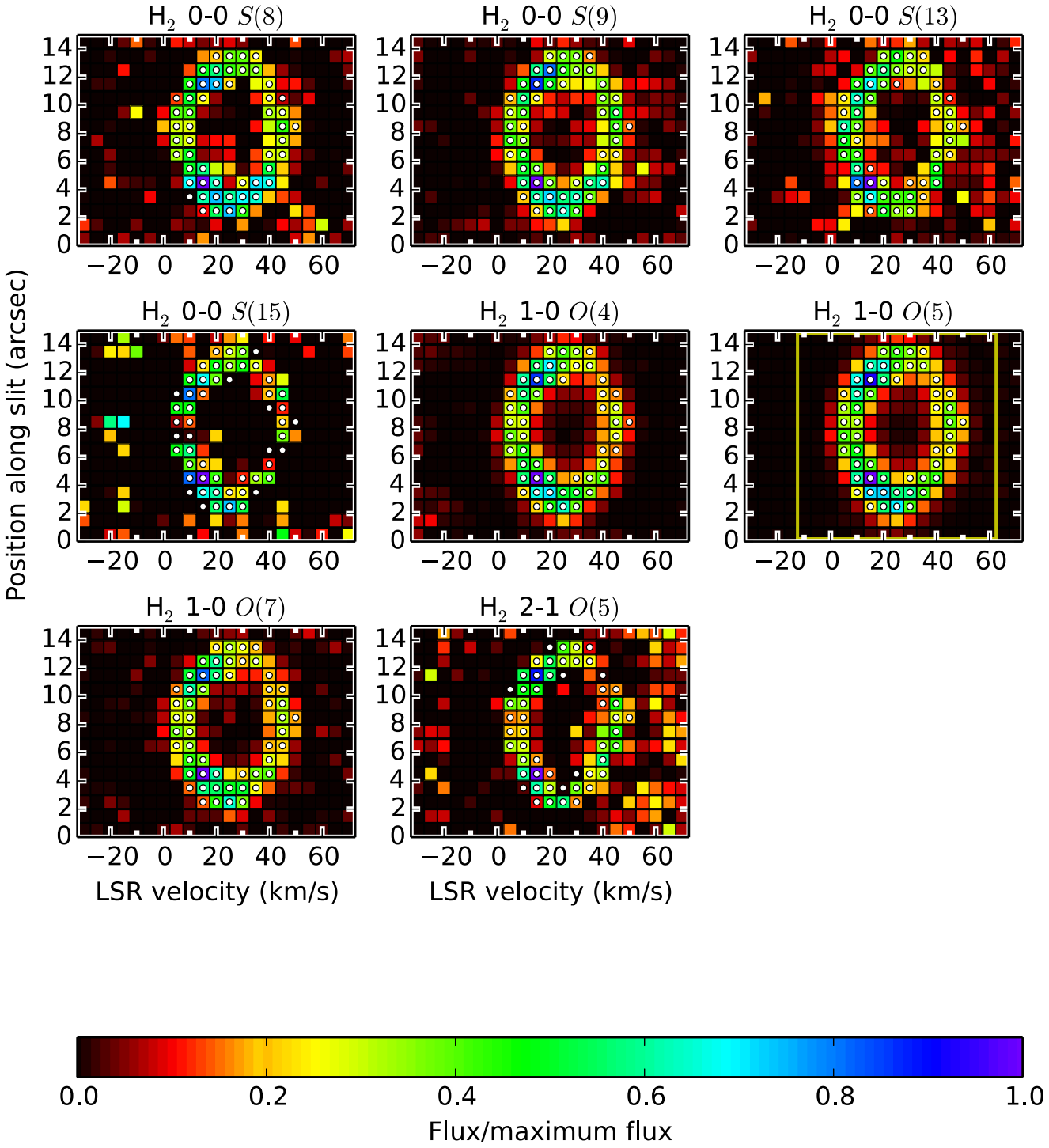

Figure 4. *P–V* diagrams for the H_2 lines. The maximum intensities for each line are given in Table 2. Yellow rectangle: region used to determine the velocity-integrated flux for the $v = 1-0$ $O(5)$ line. White circles: pixels used for flux determinations for other lines (with $v = 1-0$ $O(5)$ as a template; see the text).

pixels marked with a white circle and then divided by 0.80 to account for the weak emission lying outside the annulus of strong emission. In the case of the CH^+ $v = 1-0$ $P(4)$ and $R(1)$ lines, however, the *P–V* diagrams show clear evidence for imperfectly subtracted sky emission covering part of the relevant velocity range; for these lines, part of the 46-pixel annulus was therefore excluded in determining their ratios to the CH^+ $v = 1-0$ $P(5)$ line. Values of the estimated line fluxes are given in Table 1, together with their 1σ statistical uncertainties. For the subset of lines detected in the 2019 observations, the fluxes differ somewhat from those tabulated in Paper I, owing to the more sophisticated analysis adopted here, and the systematic uncertainty estimates are smaller. A similar procedure was adopted for the H_2 lines shown in Figure 4, using the H_2 $v = 1-0$ $O(5)$ line as a template in place of CH^+ $v = 1-0$ $P(5)$.

One surprising behavior is immediately apparent from the CH^+ line fluxes presented in Table 1 and the spectra shown in Figure 5: the line fluxes are much larger for the *P*-branch lines than for the *R*-branch lines. Considering line pairs that originate

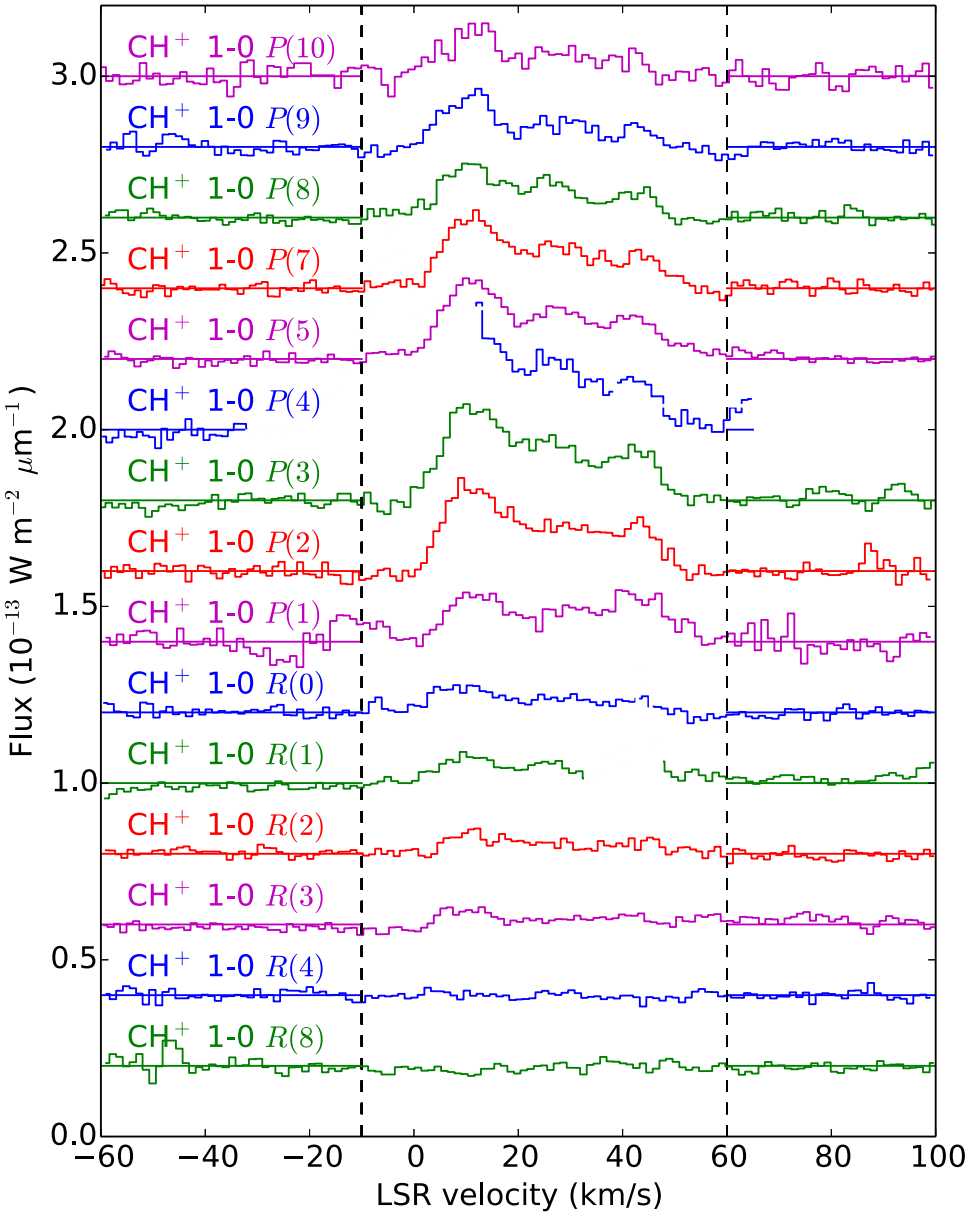

Figure 5. CH^+ line spectra, integrated along the slit.

in the same upper state, we find line flux ratios for $R(0)/P(2)$, $R(1)/P(3)$, $R(2)/P(4)$, $R(3)/P(5)$, and $R(4)/P(6)$ that are up to a factor of 30 smaller than those expected if the relative rovibronic matrix elements were simply proportional to the rotational Hönl −London factors. In the companion paper C21, this anomaly is explained beautifully by rovibronic calculations of the J-dependent transition dipole moment for the $v = 1-0$ band. The latter is found to be unusually small and shows a significant fractional change from one observed transition to the next; indeed, it passes through zero and switches sign in the vicinity of the $R(8)$ transition, and it is smaller for the R-branch transitions than for the P-branch transitions. The results presented by C21 also include the spontaneous radiative rates for rovibrational bands involving states up to $v = 4$ in the ground electronic state, $X^1\Sigma^+$, and for electronic transitions in the $A^1\Pi - X^1\Sigma^+$ band. Although vibrational bands other than $v = 1-0$ have not yet been observed, they may play an important role in the radiative cascade that populates the upper states of the transitions listed in Table 1, as will be discussed in Section 4.

3.2. Rotational Diagrams

Using the spontaneous radiative decay rates presented by C21, we obtained the rotational diagram shown in Figure 7 (top panel) for CH^+. Here, $\log_{10}[N(J_U)/g_U]$ is plotted as a function of E_U/k_B, where $N(J_U)$ is the slit-averaged column density for the $(v, J) = (1, J_U)$ upper state, $g_U = 2J_U+1$ is the degeneracy, and E_U is the energy. The column densities $N_U(J_U)$ were computed by assuming that the line emission is optically thin, a good assumption because the transition dipole moment for the $v = 1-0$ band is so small. Red points were obtained from the observed R-branch line fluxes, and blue points were obtained from the P-branch line fluxes. The black curve is the best fit obtained with the column densities taken as the sum of two components with different excitation temperatures, $T_1 \sim 115$ K and $T_2 \sim 770$ K.

In the bottom panel, the column densities are multiplied by the radiative decay rates of each state to determine the total required rate of population, P_U, in equilibrium. Results shown

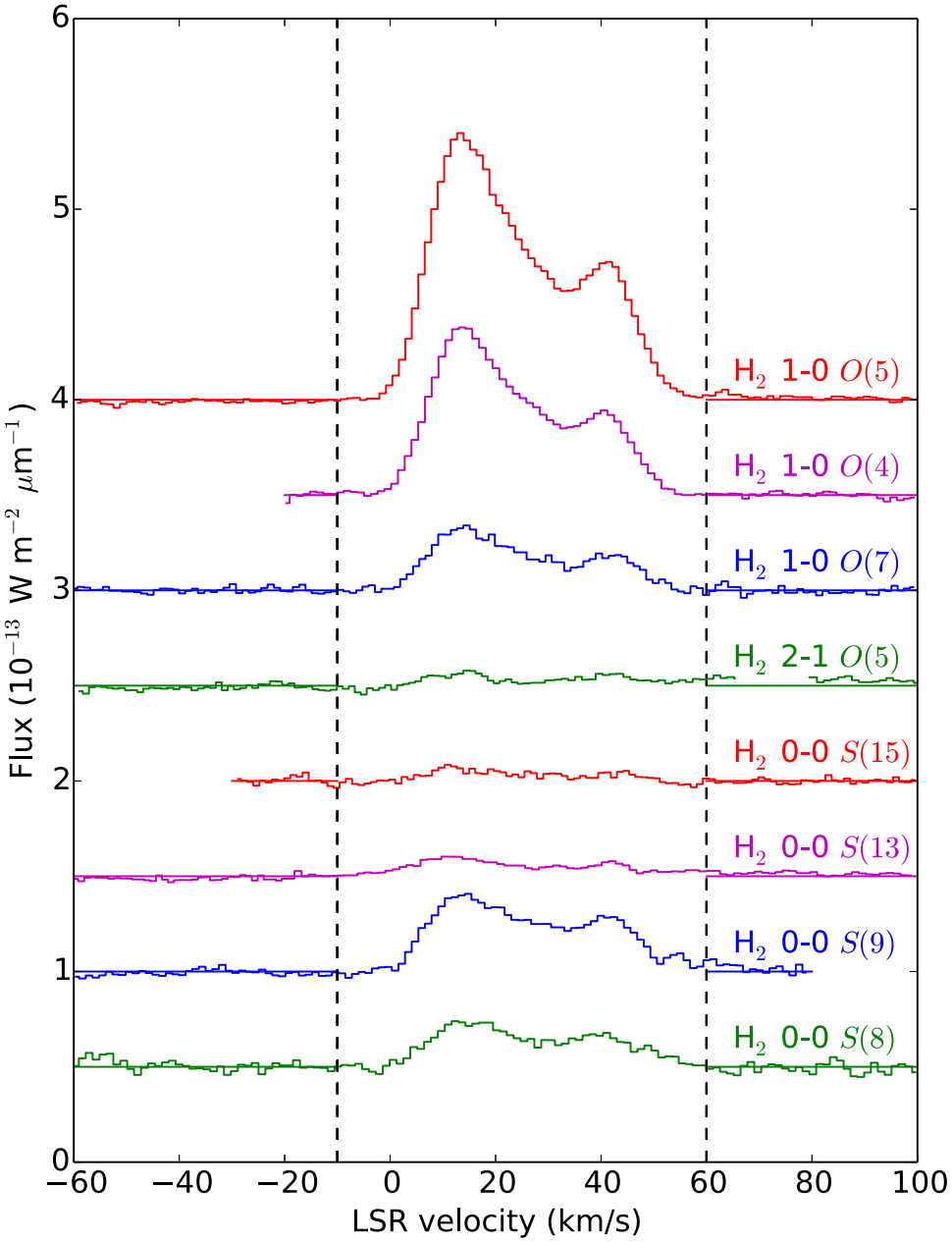

Figure 6. H_2 line spectra, integrated along the slit.

by the blue crosses include only radiative decay to the ground vibrational state: the population rates are therefore given here by $N(J_U)\ A_{10}(J_U)$, where $A_{10}(J_U)$ is the total spontaneous radiative rate from $(v, J) = (1, J_U) \rightarrow (0, J_U \pm 1)$ (i.e., including both *P*- and *R*-branch transitions). Because the vibronic transition dipole moment for the $v = 1-0$ band shows a significant dependence on J_U, $A_{10}(J_U)$ cannot be taken as a constant; thus, the blue crosses in the bottom panel show P_U/g_U declining less rapidly with E_U than does $N(J_U)/g_U$ (filled blue circles in the bottom panel). The black stars in the bottom panel show results obtained with the inclusion of radiative transitions *within the v = 1 band*: the population rates indicated by the black stars are given by $N(J_U)$ $[A_{10}(J_U)+A_{11}(J_U)]$, where $A_{11}(J_U)$ is the spontaneous radiative rate for the $(v,\ J) = (1,\ J_U) \rightarrow (1,\ J_U - 1)$ transition. These points lie above the blue crosses because they now include $v = 1-1$ transitions in the radiative loss rate; even though the $v = 1-1$ transitions are at much lower frequency than the $v = 1-0$ transitions, the dipole matrix element is much larger and $A_{11}(J_U)$ exceeds $A_{10}(J_U)$ for $J_U \geqslant 8$.

The results represented by the black stars include two contributions to the rate at which a given state is populated: the entry rate to $v = 1$, and the radiative decay rate from $(v, J) = (1, J_U + 1) \rightarrow (1, J_U)$. To determine the former alone, we make use of the expression

$$P_U = N(J_U)[A_{10}(J_U) + A_{11}(J_U)] - N(J_U + 1)A_{11}(J_U + 1). \quad (1)$$

This population rate is represented by the filled blue circles and may be considered the true entry rate to $v = 1$. As will be

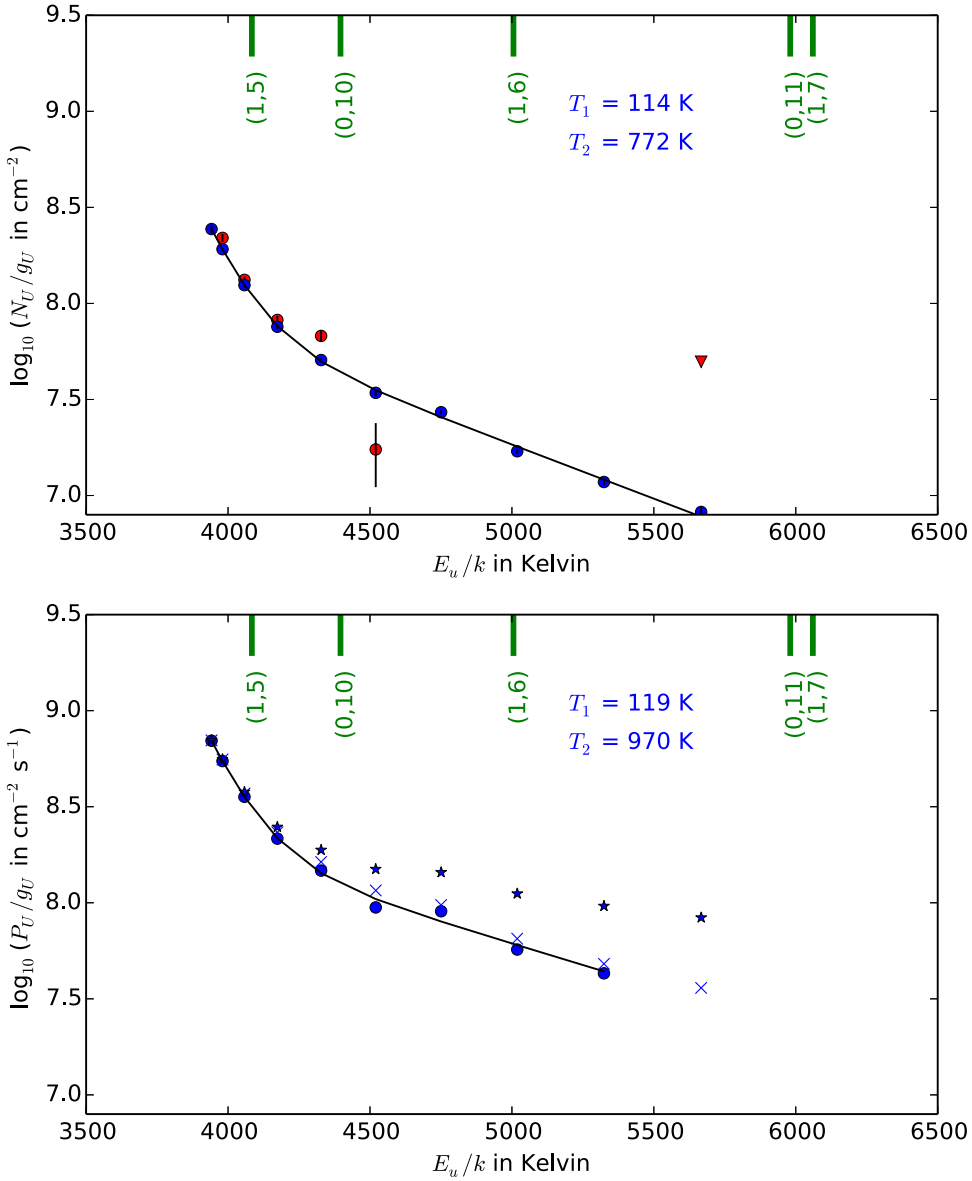

Figure 7. CH^+ rotational diagram. Top panel: column densities, with a two-component fit (black curve). Red points were obtained from the observed *R*-branch line fluxes, and blue points were obtained from the *P*-branch line fluxes. Bottom panel: pumping rates under three assumptions (see the text for details). The filled blue circles in the bottom panel represent the actual entry rates to $v = 1$, for which we obtained a two-component fit (black curve). The green bars at the top of each panel, which are labeled with the (v,J) of the reactant H_2 molecule, indicate the energies E_U above which a given reaction channel becomes endoergic (see the text for details).

discussed in Section 4 below, the population of vibrationally excited states of CH^+ is dominated by chemical (or "formation") pumping, in which the reaction of C^+ with H_2 to form CH^+ leaves CH^+ in a vibrationally excited state. The filled blue circles in the bottom panel therefore represent the rate of chemical pumping. As in the top panel, we fitted the blue circles representing P_U/g_U by the sum of two thermal distributions at different temperatures: the best-fit values were $T_1 \sim 120$ K and $T_2 \sim 970$ K.

The green bars at the top of each panel, which are labeled with the (v, J) of the reactant H_2 molecule, indicate the energies E_U above which a given reaction channel becomes endoergic. In other words, the reaction of $H_2(v, J)$ with C^+ to form an excited state of CH^+ with energy E_U is exoergic for E_U to the left of the green bar labeled with (v, J) and endoergic to the right.

In Figure 8, we show the rotational diagram for the observed transitions of H_2. Once again, the black curve is the best fit obtained with the column densities taken as the sum of two components with different excitation temperatures, in this case $T_1 \sim 1130$ K and $T_2 \sim 2430$ K. Red, blue, and white symbols refer to states with $v = 0$, 1, and 2, respectively; triangles represent states of ortho-H_2 (i.e., with J_U odd), and circles represent states of para-H_2 (J_U even). Overall, a simple two-temperature model yields a reasonably good fit to all the observed line fluxes, regardless of vibrational state.[10]

[10] One systematic deviation from the fit is that the column densities of para-H_2 states in $v = 1$ are slightly elevated relative to the ortho-H_2 states, implying that the ortho-to-para ratio in $v = 1$ is smaller than the value of 3 expected in local thermodynamic equilibrium. As discussed by Sternberg & Neufeld (1999), this behavior can be readily understood as being the result of differential shielding in the optically thick ultraviolet transitions that pump the $v = 1-0$ band of H_2.

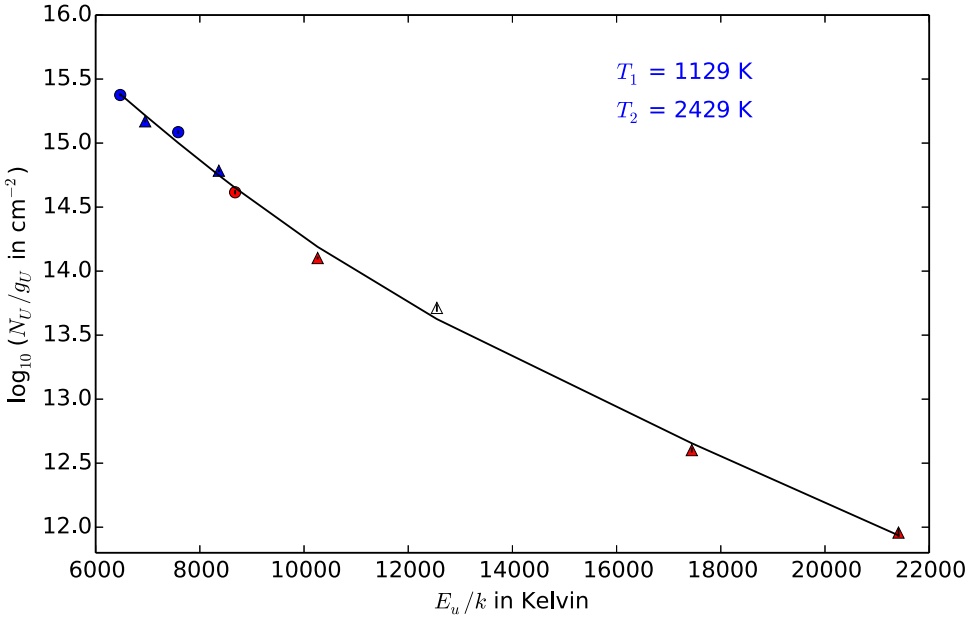

Figure 8. H_2 rotational diagram. Red, blue, and white symbols refer to states with $v = 0$, 1, and 2, respectively; triangles represent states of ortho-H_2 (i.e., with J_U odd), and circles represent states of para-H_2 (J_U even); the black line is a two-component fit.

4. Model for the Excitation of CH^+

Our chemical and excitation model for CH^+ updates the model described by Godard & Cernicharo (2013, hereafter GC13) and extends it to include predictions for the rovibrational lines. The GC13 model, which includes CH^+ excitation by formation pumping, collisional excitation, and radiative pumping at optical and infrared wavelengths, was successfully used to model CH^+ pure rotational emissions detected from NGC 7027 (Cernicharo et al. 1997). The chemistry, excitation, and radiative transfer of CH^+ are computed here with the latest version of the Meudon photodissociation region (PDR) code[11] (e.g., Le Petit et al. 2006) modified to treat the entire energetic structure of CH^+ and all excitation and de-excitation processes. In this section, we describe updates to the treatment of the fundamental physical processes of relevance.

4.1. CH^+ Energy Structure and Spectroscopy

As in GC13, we include all rovibrational levels with $v \leqslant 4$ and $J \leqslant 30$ within the ground electronic state $X^1\Sigma^+$ and the first electronic state $A^1\Pi$ of CH^+. The corresponding energies are derived from the spectroscopic parameters of Hakalla et al. (2006) and range up to $E/k_B \sim 50{,}000$ K (see GC13, their Figure 1). To take into account the centrifugal distortion-induced interference effects described by C21, the spontaneous decay rates of allowed electronic and rovibrational transitions of CH^+ are calculated using the polynomial fits to the m-dependent dipole moments derived by C21. This approach differs considerably from the prescription used in GC13, where radiative decay rates were calculated under the Born–Oppenheimer and r-centroid approximations using the Franck-Condon factors and the r-centroids of Hakalla et al. (2006).

With these new data in hand, the infrared pumping of the rovibrational levels of the $X^1\Sigma^+$ state is computed using the escape probability formalism. In contrast, the optical pumping of the $A^1\Pi$ electronic state, followed by the subsequent fluorescent cascade in the ground state, is treated using pumping matrix elements under the approximation that the de-excitation of any electronic level is dominated by the radiative decay to the $X^1\Sigma^+$ state. Self-shielding processes within the electronic lines of CH^+ at optical wavelengths are calculated using the FGK approximation (Federman et al. 1979).

4.2. Collisional Excitation

Inelastic nonreactive collisional processes are included taking into account H, H_2, He, and e^- as collision partners and using the rates and prescriptions described in Appendix B. Because it is a short-lived species, CH^+ can be highly sensitive to formation pumping mechanisms. Indeed, in hot and dense PDRs, the ion–neutral reaction

$$C^+ + H_2(v, J) \rightarrow CH^+(v', J') + H \quad (2)$$

is found to be not only the dominant pathway for the formation of CH^+ (e.g., Agúndez et al. 2010) but also a major process for the excitation of its pure rotational levels (e.g., GC13; Faure et al. 2017). To account for this effect, we include the detailed treatment of the above state-to-state chemical reactions described in Appendix B.[12]

4.3. Geometrical Model and Radiative Transfer

The modeling of H_2 and CH^+ emissions in NGC 7027 is performed in two steps as schematized in Figure 9. The thermal, chemical, and excitation profiles of the neutral gas are computed with the Meudon PDR code in a plane-parallel

[11] Version 1.5.4 available on the ISM platform https://ism.obspm.fr.

[12] We have also considered the reaction $C^{++} + H_2 \rightarrow CH^+ + H^+$ as a possible source of CH^+ formation and excitation within the photoionized region that lies interior to the PDR. Here, we adopted an upper limit on the rate coefficient presented recently by Plašil et al. (2021) and used the CLOUDY photoionization model (Ferland et al. 2017) to determine the expected C^{++} and H_2 abundances. Even if every reaction of C^{++} and H_2 leads to a vibrationally excited CH^+ molecule, the resultant total rovibrational line flux lies at least 4 orders of magnitude below the measured value. This possible production mechanism can therefore be excluded robustly.

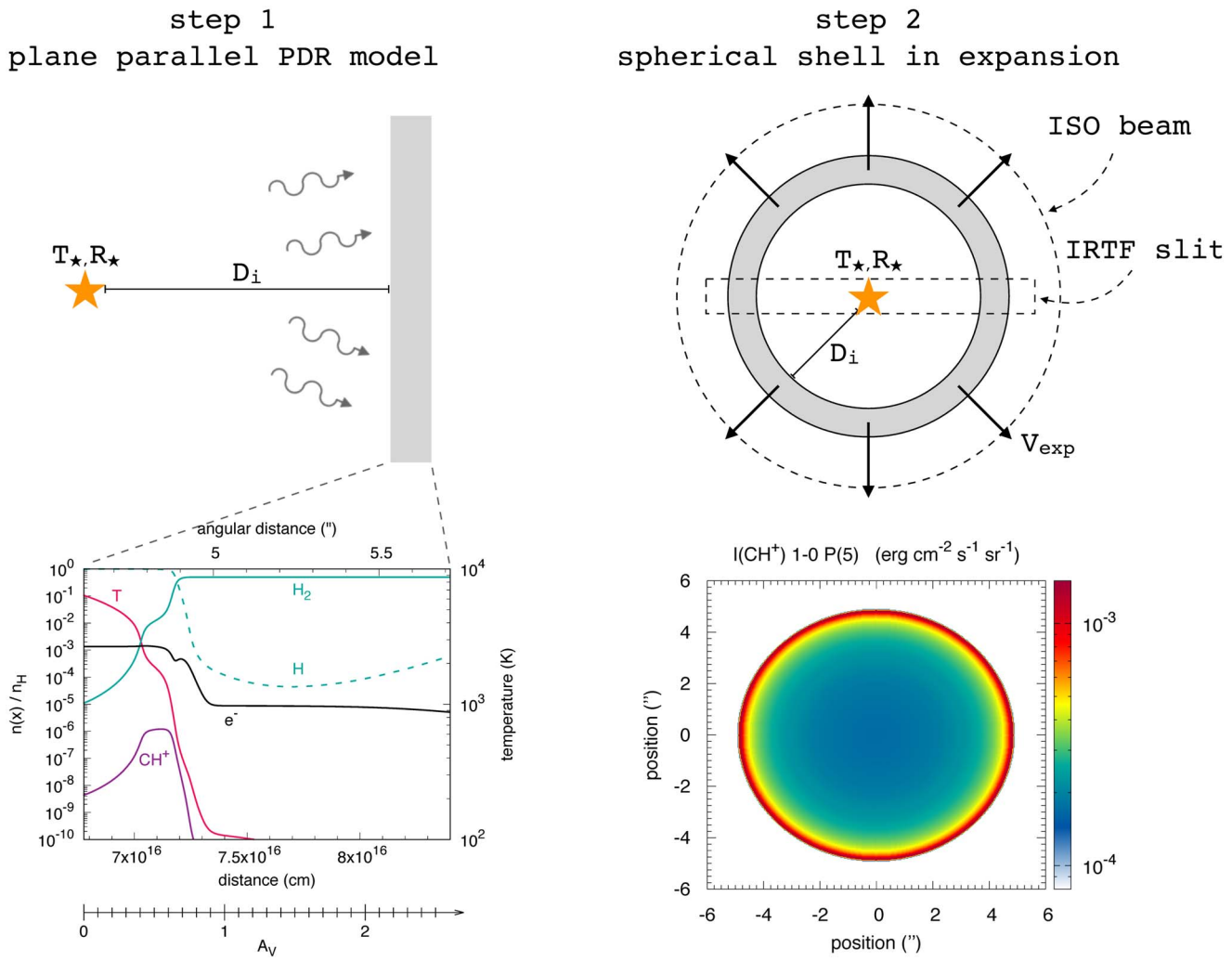

Figure 9. Summary of the modeling strategy. Top left: the thermochemical and excitation profiles of a neutral slab of gas illuminated on one side by a star are calculated in a plane-parallel geometry. Bottom left: kinetic temperature T and abundances of H, H_2, e^-, and CH^+ obtained for an isochoric PDR with a density $n_H = 3 \times 10^5$ cm^{-3} as functions of the distance to the star, starting from the ionization front. (Results for an isochoric PDR with this density, obtained from the earlier model of GC13, are shown in their Figure 6.) Top right: the radiative transfer within the rovibrational lines of H_2 and CH^+ is computed by wrapping the PDR around a sphere of radius D_i expanding at a constant velocity V_{exp}. Bottom right: example of the intensity map obtained for the 1−0 $P(5)$ line of CH^+.

geometry, taking into account all the processes described in the previous section (bottom left panel of Figure 9). As in Paper I and following Zijlstra et al. (2008), we assume a distance to the source of 980 pc. The PDR is assumed to be illuminated from one side by a blackbody generated by a star with an effective temperature $T_\star = 198{,}000$ K and a radius $R_\star = 5.21 \times 10^9$ cm (Latter et al. 2000) located at a distance $D_i = 0.022$ pc from the ionization front (see Paper I). To correctly model the self-shielding and the UV pumping of the electronic lines of H_2, the radiative transfer within the Lyman and the Werner bands of H_2 is computed self-consistently with an exact treatment rather than with the FGK approximation. Chemical and excitation profiles are computed up to a visible extinction $A_{V\,\max} = 10$.

To mimic a spherical shell in expansion at a constant radial velocity V_{exp}, the resulting PDR is then wrapped around a sphere of radius D_i (top right panel of Figure 9). The radiative transfer in the rovibrational lines of H_2 and CH^+ is solved within this geometry for 200 values of the impact parameter homogeneously spread up to the outer shell, taking into account the Doppler shift and the Doppler broadening induced by the expansion and a turbulent velocity dispersion σ_{turb}. The resulting line profiles are variously integrated in order to derive intensity maps (bottom right panel of Figure 9), P–V diagrams, and line fluxes collected over the Infrared Space Observatory (ISO) beam or the IRTF slit (shown with dashed lines in the top right panel of Figure 9).

4.4. Main Parameters

The PDR is modeled as an isochoric or isobaric environment neglecting the dilution of the expanding gas along the radial direction. This approximation is supported by the fact that the width of the neutral shell responsible for H_2 and CH^+ rovibrational emissions relative to its distance from the central star never exceeds 20% in all our models (see, e.g., the bottom left panel of Figure 9). As described above, the radiation conditions are derived from the observed properties of the central star of NGC 7027. Following GC13, the carbon-rich circumstellar envelope is modeled with C, O, N, and S gas-phase elemental abundances of 1.3×10^{-3}, 5.5×10^{-4},

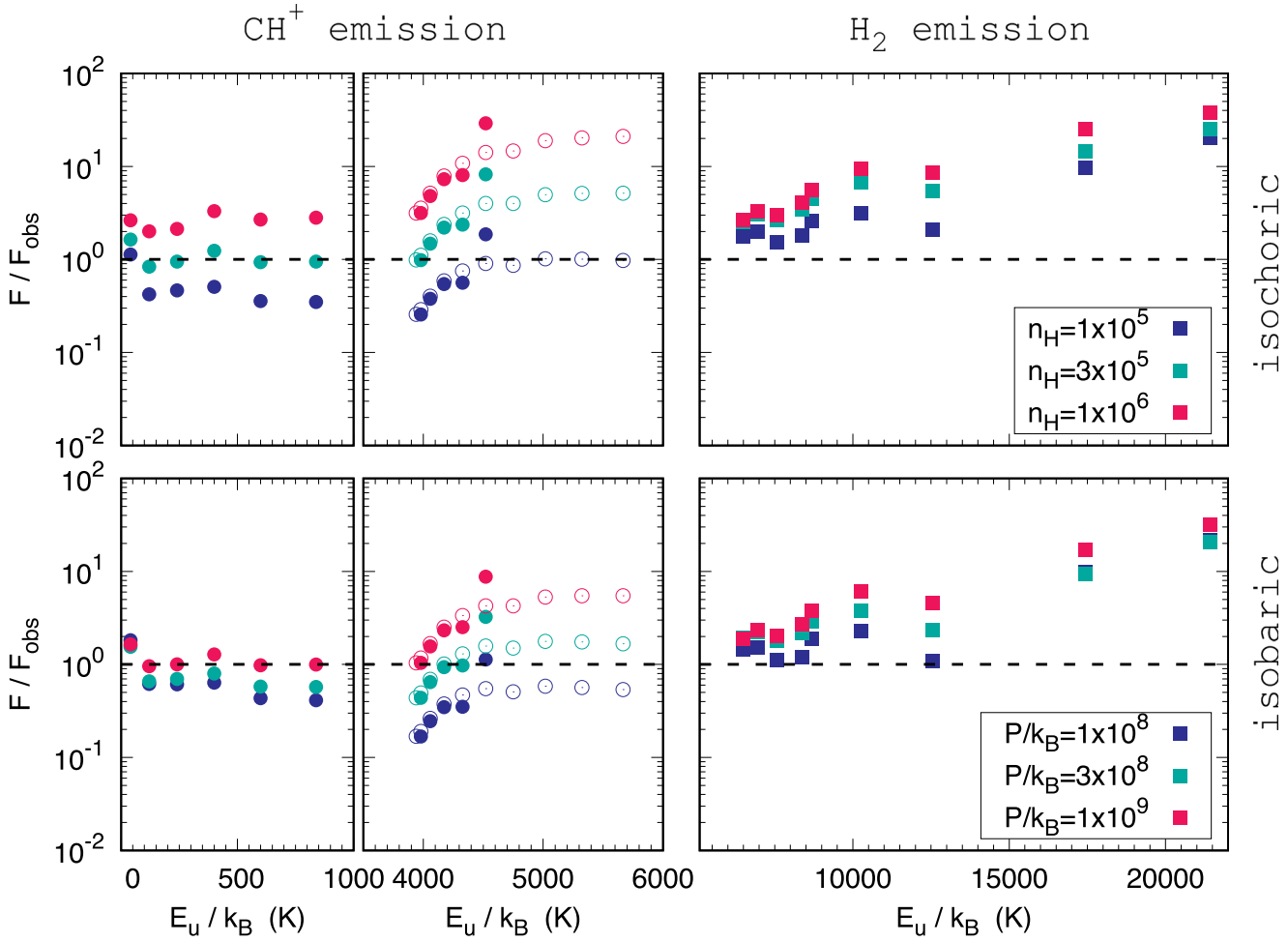

Figure 10. Ratios of predicted to observed fluxes $F/F_{\rm obs}$ computed for the pure rotational lines of CH^+ (left panel), the rovibrational lines of CH^+ (middle panel), and the rovibrational lines of H_2 (right panel) as functions of the energies E_u / k_B of the upper levels of the transitions. The models include isochoric PDRs (top panels) with $n_{\rm H} = 10^5$, 3×10^5, and 10^6 cm^{-3} and isobaric PDRs (bottom panels) with $P/k_B = 10^8$, 3×10^8, and 10^9 K cm^{-3}. R-branches and P-branches are shown with filled and open circles, respectively. Simulated fluxes are obtained by integrating the line intensities over the instrumental beam (see text for details).

1.9×10^{-4}, and 7.9×10^{-6}, respectively (Middlemass 1990). We adopted a PAH-to-dust mass ratio of 1.5% (Lau et al. 2016). The density $n_{\rm H}$ (for isochoric models) and the thermal pressure P (for isobaric models) are left as free parameters.

Interestingly, despite the fact that the elemental abundances in carbon-rich evolved stars differ markedly from those in ordinary PDRs, a first estimate of the PDR density (or pressure) can be obtained using the ISMDB Inverse Search Service,[13] which performs comparisons of observational data with precomputed grids of PDR models. Applying this tool to the mean intensity of the rovibrational lines of H_2 (Table 2) yields a PDR with a density $n_{\rm H} \sim 10^5$ cm^{-3} (or a pressure $P/k_B \sim 2 \times 10^8$ K cm^{-3}) illuminated by a standard interstellar radiation field scaled by a factor $G_0 \sim 10^5$, in excellent agreement with the values obtained with the model of GC13 and the UV energy density expected at a distance $D_i = 0.022$ pc from the central star of NGC 7027. In the following, we therefore explore the results of our model for several values of the density and thermal pressure centered around these preliminary estimates.

[13] https://ismdb.obspm.fr

5. Comparison between the Model Predictions and the Observations

5.1. CH^+ and H_2 Line Fluxes

A comparison between the predicted and the observed line fluxes of CH^+ and H_2 is shown in Figure 10, which displays the results obtained for isochoric and isobaric PDRs at different densities and thermal pressures, assuming a turbulent velocity dispersion $\sigma_{\rm turb} = 6$ km s^{-1}. To match the various observational setups, the fluxes of the pure rotational lines of CH^+ are integrated over a circular aperture with a diameter of 37″ ($J = 1 - 0$, observed with Herschel/SPIRE by Wesson et al. 2010) or 85″ (other pure rotational transitions, observed with ISO by Cernicharo et al. 1997), while those of the rovibrational lines of CH^+ and H_2 are integrated over a slit of size 0.″375×15″ (see Figure 9).

Over the entire grid of models, the excitation of the high-energy pure rotational levels of CH^+ ($J \gtrsim 4$) and the excitation of all its rovibrational levels are dominated by formation pumping. In particular, nonreactive collisional excitation of the $v = 1$ levels is found to be at least one order of magnitude less efficient than formation pumping even if the scaling applied for collisional transition between vibrational levels (i.e., the a coefficient in Equation (B4)) is set to 1. Similarly, and in line

with the results of GC13, the radiative pumping of the first electronic state of CH^+ has a weak contribution. Because the stellar radiation field follows a Planck law at high temperature, the energy density at optical wavelengths is negligible compared to the UV energy density and at least 100 times too small to make the radiative pumping a dominant source of excitation of CH^+.

The fraction of the incident UV flux that is reprocessed into rovibrational lines of H_2 depends on the density of the PDR. Because the excitation of the lower rotational levels of H_2 varies nonlinearly with the density and temperature, the self-shielding of H_2 is less efficient at higher densities; hence, the radiative pumping of the rovibrational lines of H_2 extends over larger column densities when the density is higher.

Since both the formation of CH^+ and its excitation result from state-to-state chemistry involving molecular hydrogen, the dependence of CH^+ emission on the gas density is even stronger. As previously shown by GC13, we find that an isochoric PDR with a density $n_H = 3 \times 10^5$ cm^{-3} almost perfectly reproduces the observed fluxes of all the pure rotational lines of CH^+, with discrepancies smaller than a factor of 1.5. However, such a model overestimates the emissions of several rovibrational lines of CH^+ by a factor of 4 to 6 and those of the rovibrational lines of H_2 by a factor of 3 to ~30. In contrast, we find that an isobaric PDR with a thermal pressure $P/k_B = 3 \times 10^8$ K cm^{-3} is able to reproduce simultaneously the emissions of most of the rovibrational lines of CH^+ and H_2 within a factor of 2 to 3, with the exception of the 0−0 S(15) and S(13) lines of H_2. Interestingly, the first two pure rotational transitions of CH^+ are optically thick, and thus their line strengths depend strongly on the turbulent velocity dispersion σ_{turb}. Reproducing the observed intensities of these two lines with the optimal isochoric or isobaric models requires 6 km s^{-1} $\leqslant \sigma_{turb} \leqslant$ 8 km s^{-1}, in good agreement with the velocity dispersion derived from the wings of CH^+ and H_2 spectra (see Figures 5 and 6).

5.2. Position–Velocity Diagrams

The P–V diagram for the 1−0 $P(5)$ line of CH^+ predicted along the observational slit is shown in Figure 11. The optimal isochoric (or isobaric) model explains remarkably well the shape and both the spatial and spectral extents of the ring-like profile described in Section 3, provided that the spherical shell expands at a velocity $V_{exp} = 20$ km s^{-1}. Unsurprisingly, the model also predicts strong emission at the systemic velocity of the source. This is a direct consequence of the limb-brightening effect and of the simplicity of the modeling. In the single plane-parallel PDRs modeled here, the size d of the region responsible for the emission of CH^+ and H_2 is small compared to the distance of the neutral cloud to the central star D_i. When wrapped in a spherical geometry, the limb-brightening effect, i.e., the enhanced emission of the border of the sphere compared to the center, scales as

$$\sqrt{\frac{2D_i}{d} + 1}\,, \tag{3}$$

leading to strong variations of the intensity both in space (Figure 9) and in velocity (Figure 11). This result strongly contrasts with the observations that indicate that the emission of CH^+ and H_2 is less strongly limb brightened (see Figures 2–4). Since the excitation conditions of CH^+ and H_2 cannot be explained by a medium at low density ($\leqslant 10^5$ cm^{-3}), which would naturally yield a thicker shell with less limb brightening, this discrepancy implies that the geometrical model is too simplistic. A second, related discrepancy concerns the relative spatial extents of the different lines that were observed. While we detected no measurable differences between the spatial extents of the various CH^+ $v = 1$−0 transitions, in agreement with the model predictions, the line emissions from H_2 have a slightly greater spatial extent than those from CH^+ (as is evident from a comparison of Figures 2 and 4). The model, however, predicts a P−V diagram for the H_2 line that is indistinguishable from that observed for CH^+ (Figure 11, top panel). These discrepancies suggest that the neutral shell of NGC 7027 should ultimately be modeled in a nonspherical and inhomogeneous geometry following the complex three-dimensional structure of the nebula derived by

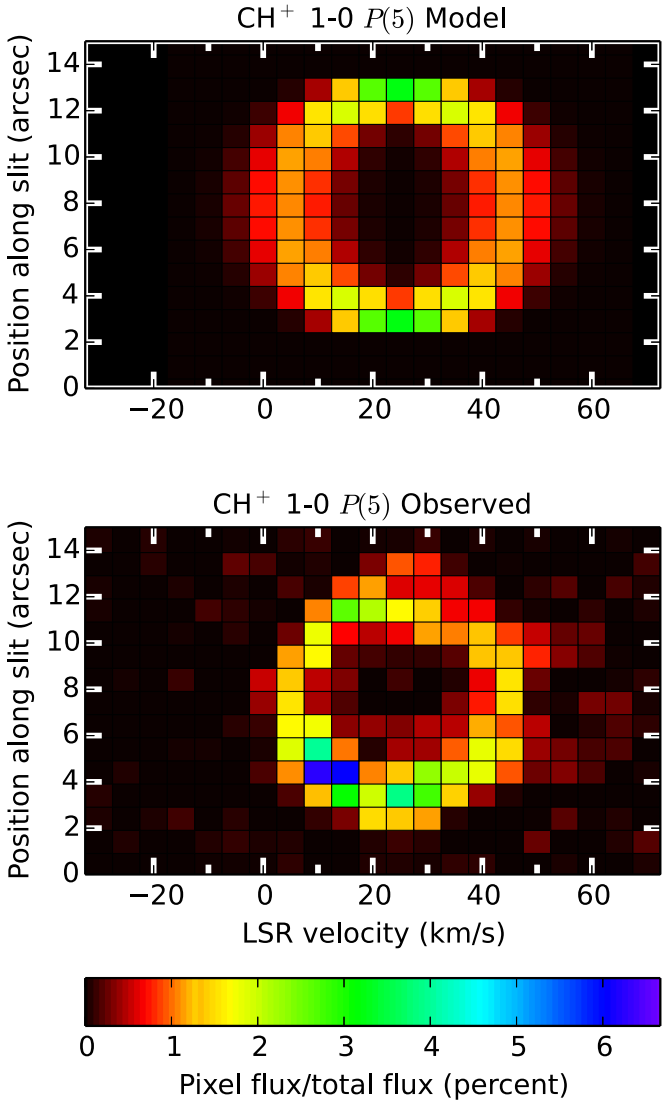

Figure 11. Top panel: specific intensity of the 1−0 $P(5)$ line of CH^+ computed using an isochoric PDR model with $n_H = 3 \times 10^5$ cm^{-3} wrapped around a sphere expanding at a velocity $V_{exp} = 20$ km s^{-1} as a function of the velocity and the position along a slit identical to the observational setup. Intensities are averaged over a spatial bin of 1″ and a spectral bin of 5 km s^{-1} as in Figures 2–4. The source was assumed to have a centroid v_{LSR} of 25 km s^{-1} with its center at +8″. Bottom panel: observed P−V diagram for CH^+ 1−0 $P(5)$.

Cox et al. (2002), for example. Such an analysis is beyond the scope of the present work.

5.3. CH^+ Rovibrational Emissions as a Tracer of Warm, Dense UV-irradiated Gas

The models presented here suggest that CH^+ rovibrational emissions are a tracer of warm ($T \sim 1000$ K), dense ($n_H \sim 3 \times 10^5$ cm^{-3}) UV-irradiated gas. The critical pathway for the excitation of these emissions is the reaction of C^+, produced by photoionization, and excited H_2 in states with $E/k_B \gtrsim 8000$ K. In UV-irradiated gas, excited H_2 is produced both by radiative pumping through the Lyman and Werner bands and by collisional excitation in the warm UV-heated gas; at densities above $\sim 10^5$ cm^{-3} (Sternberg & Dalgarno 1989), the latter process is typically dominant in populating the lower-energy ($E/k_B \leqslant 15{,}000$ K) excited states that are most important for CH^+ formation. Dense PDRs (unassociated with evolved stars) and UV- and self-irradiated shock waves (e.g., Godard et al. 2019, Lehmann et al. 2020) are other environments in which CH^+ rovibrational emissions are potentially detectable; the required conditions are especially prevalent in starburst galaxies (e.g., Falgarone et al. 2017).

6. Summary

(1) Observations in the 3.49–4.13 μm spectral region, conducted with the iSHELL spectrograph on NASA's Infrared Telescope Facility (IRTF) on Maunakea, have resulted in the unequivocal detection of the $R(0)-R(3)$ and $P(1)-P(10)$ transitions within the $v = 1-0$ band of CH^+. Nine infrared transitions of H_2 were also detected in these observations, comprising the $S(8)$, $S(9)$, $S(13)$, and $S(15)$ pure rotational lines; the $v = 1-0$ $O(4)-O(7)$ lines; and the $v = 2-1$ $O(5)$ line.

(2) The R-branch transitions are anomalously weak relative to the P-branch transitions, a behavior that is explained accurately by rovibronic calculations of the transition dipole moment reported in a companion paper (Changala et al. 2021).

(3) We presented a photodissociation model that includes a detailed treatment of the excitation of CH^+ by inelastic collisions, optical pumping, and chemical ("formation") pumping.

(4) Chemical pumping, resulting from the formation of CH^+ in excited rovibrational states following the reaction of C^+ with H_2, is found to completely dominate the excitation of the vibrational transitions reported here.

(5) The model is remarkably successful in explaining both the absolute and relative strengths of the CH^+ and H_2 lines.

The observations reported here were carried out at the Infrared Telescope Facility (IRTF), which is operated by the University of Hawaii under contract NNH14CK55B with the National Aeronautics and Space Administration. We are very grateful to the IRTF director, John Rayner, for making unallocated engineering time available for the 2019 July observations that initiated this project. We thank the IRTF support astronomers and telescope operators for the excellent support they provided for the observations reported here. The grids of models have been run on the computing cluster Totoro funded by the European Research Council, under the European Community's Seventh framework Programme, through the Advanced Grant MIST (FP7/2017-2022, No. 742719). M.G. is supported by the German Research Foundation (DFG) grant GO 1927/6-1. P.B.C. is supported by NSF grant AST-1908576. T.R.G.'s research is supported by the international Gemini Observatory.[14] We thank Holger Müller for useful discussions and the anonymous referee for several helpful suggestions. Finally, we are particularly grateful to Miwa Goto, who expertly led the acquisition of the data at the IRTF.

Appendix A
Decomposition of Blended Spectral Features

The CH^+ $v = 1-0$ $P(6)$ line at 3.907767 μm is blended with the nearby 3.907549 μm $n = 15-6$ recombination line of atomic hydrogen. To decompose the blended feature, we fit the observed P–V diagram as a linear combination of those obtained for two unblended lines: those of the H I $n = 14-6$ line and the CH^+ $v = 1-0$ $P(5)$ line, with the latter shifted as appropriate to reflect the difference between the CH^+ $v = 1-0$ $P(6)$ and H I $n = 15-6$ rest wavelengths. The coefficients in the linear combination were adjusted to optimize the fit to the data, yielding an estimated CH^+ $v = 1-0$ $P(6)/P(5)$ line ratio of 0.927. Figure 12 illustrates this deblending procedure. Here, the top row shows P–V diagrams for the blended feature and the optimally scaled H I $n = 14-6$ and CH^+ $v = 1-0$ $P(5)$ lines (Components A and B). The middle row shows the sum of Components A and B (left column) and the difference between the P–V diagrams for the blended feature and those for Components B (middle column) and A (right column). The optimal scaling we adopted therefore minimizes the differences between each P–V diagram in the middle row and the P–V diagram immediately above it. The bottom left panel shows the residuals in the fit, i.e., the difference between the observed blended feature and the sum of Components A and B.

The H_2 $v = 1-0$ $O(6)$ line at 3.500809 μm is blended with the nearby 3.501164 μm $n = 24-6$ recombination line of atomic hydrogen. We adopted a similar deblending procedure to that described above, but now using a linear combination of the $P-V$ diagrams for H_2 $v = 1-0$ $O(5)$ and H I $n = 25-6$. This procedure is illustrated in Figure 13.

[14] A program of NSF's NOIRLab, which is managed by the Association of Universities for Research in Astronomy (AURA) under a cooperative agreement with the National Science Foundation, on behalf of the Gemini Observatory partnership: the National Science Foundation (United States), National Research Council (Canada), Agencia Nacional de Investigación y Desarrollo (Chile), Ministerio de Ciencia, Tecnología e Innovación (Argentina), Ministério da Ciência, Tecnologia, Inovações e Comunicações (Brazil), and Korea Astronomy and Space Science Institute (Republic of Korea).

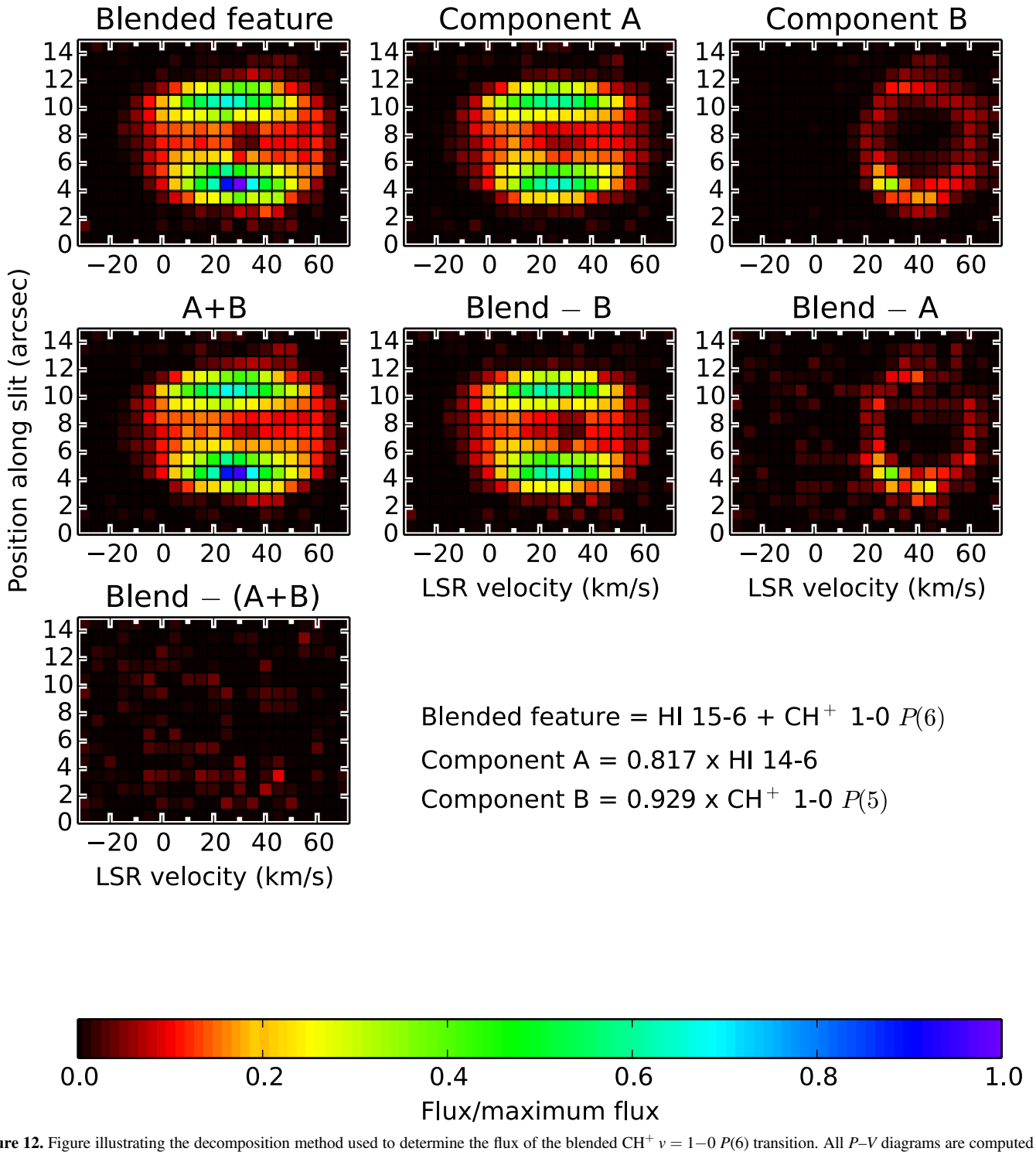

Figure 12. Figure illustrating the decomposition method used to determine the flux of the blended CH^+ $v = 1-0$ $P(6)$ transition. All P–V diagrams are computed for the rest frequency of the H I $n = 15-6$ transition, and thus the LSR velocity refers to Component A. Details are described in the text.

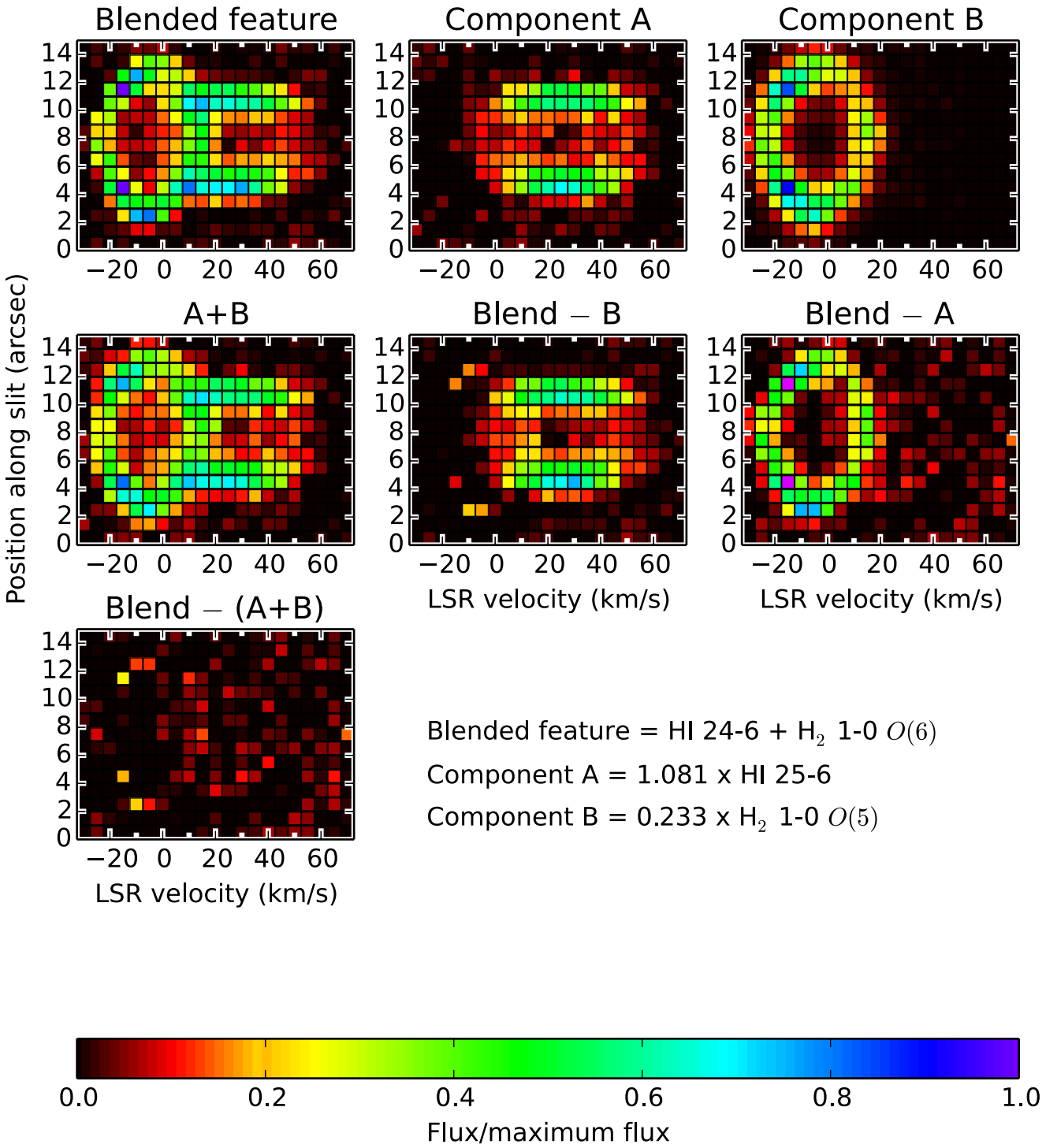

Figure 13. Figure illustrating the decomposition method used to determine the flux of the blended H_2 $v = 1-0$ $O(6)$ transition. All P–V diagrams are computed for the rest frequency of the H I $n = 25-6$ transition, and thus the LSR velocity refers to Component A. Details are described in the text.

Appendix B
Collisional Excitation of CH^+

B.1. Nonreactive Collisional Excitation

For the collisional excitation of CH^+ within the ground vibrational state by e^- and H, we adopt the data of Hamilton et al. (2016) and Faure et al. (2017), who provided de-excitation rates for states up to $J_{max} = 18$ (A. Faure, private communication). For collisions with He, we use the de-excitation rates computed by Hammami et al. (2009) for states up to $J_{max} = 10$. Collisional rates for CH^+ with H_2 are derived from those of CH^+ with He using the rigid rotor approximation.

The above de-excitation rate coefficients are used for any transition $v', J' \rightarrow v'', J''$ such that $v' = v'' = 0$ and $J' \leqslant J_{max}$. The de-excitation rate coefficient $k^{C}_{v'J'v''J''}$ of other rotational or vibrational transitions is computed as

$$k^{C}_{v'J'v''J''} = k^{C}(T)\, f_{v'J'v''J''}\,, \tag{B1}$$

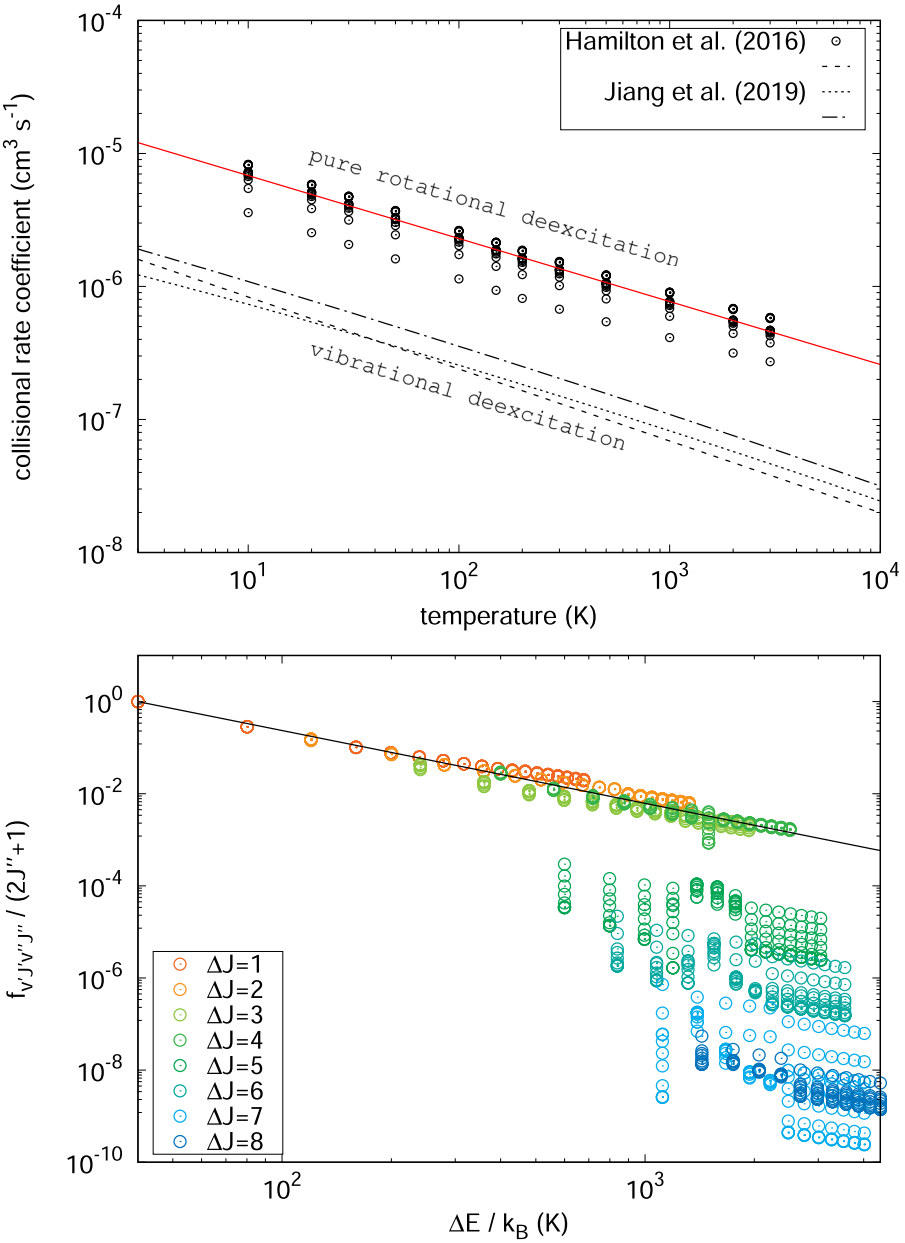

Figure 14. Top: total collisional de-excitation rate coefficients for CH^+ in collisions with e^-. Open circles correspond to de-excitation of pure rotational levels (Hamilton et al. 2016). Black curves correspond to vibrational de-excitation of the $v' = 1$ (dashed), $v' = 2$ (dotted), and $v' = 3$ (dotted-dashed) levels of CH^+ (Jiang et al. 2019). The red curve shows a fit of pure rotational data using Equation (B3) with $\alpha = -4.7$, $\beta = -0.47$, and $\gamma = 0$. Bottom: probability distribution of rotational de-excitation as a function of the level energy difference ΔE and ΔJ (Hamilton et al. 2016). The black curve indicates the power-law fit used in Equation (B4).

where $k^{\rm C}(T)$ is the total de-excitation rate coefficient, which we assume identical for all levels v', J' and consider to only depend on the kinetic temperature T, and $f_{v'J'v''J''}$ is a distribution function over lower levels such that

$$\sum_{v'',J''} f_{v'J'v''J''} = 1 \quad \forall\ v',\ J'. \tag{B2}$$

The total de-excitation rate coefficient $k^{\rm C}(T)$ is obtained by performing a second-order polynomial fit in logarithmic space to the total de-excitation rates for pure rotational levels,

$$k^{\rm C}(T) = 10^{\alpha}\ 10^{\beta\ \log(T)}\ 10^{\gamma\ \log^2(T)}. \tag{B3}$$

We assume that the distribution function $f_{v'J'v''J''}$ can be approximated as

$$f_{v'J'v''J''} = a(\Delta v)\, b(\Delta J)(2J'' + 1)\, \Delta E^c, \tag{B4}$$

i.e., follows a power dependence on the level energy difference ΔE with scaling coefficients a and b that solely depend on $\Delta v = v' - v''$ and $\Delta J = J' - J''$, respectively. The power-law dependence on ΔE is deduced from a fit to the pure rotational collisional rates. The b coefficients are set to reproduce the dependence on ΔJ of pure rotational transition for $\Delta J \leqslant \Delta J_{\rm max}$ and set to 0 for $\Delta J > \Delta J_{\rm max}$. Here, $\Delta J_{\rm max} = 18$, 8, and 10, respectively, for collisions with H, e^-, and He. The a coefficients are set to 1 for $\Delta v = 0$ and to 0.1 for $\Delta v \neq 0$ in order to reproduce

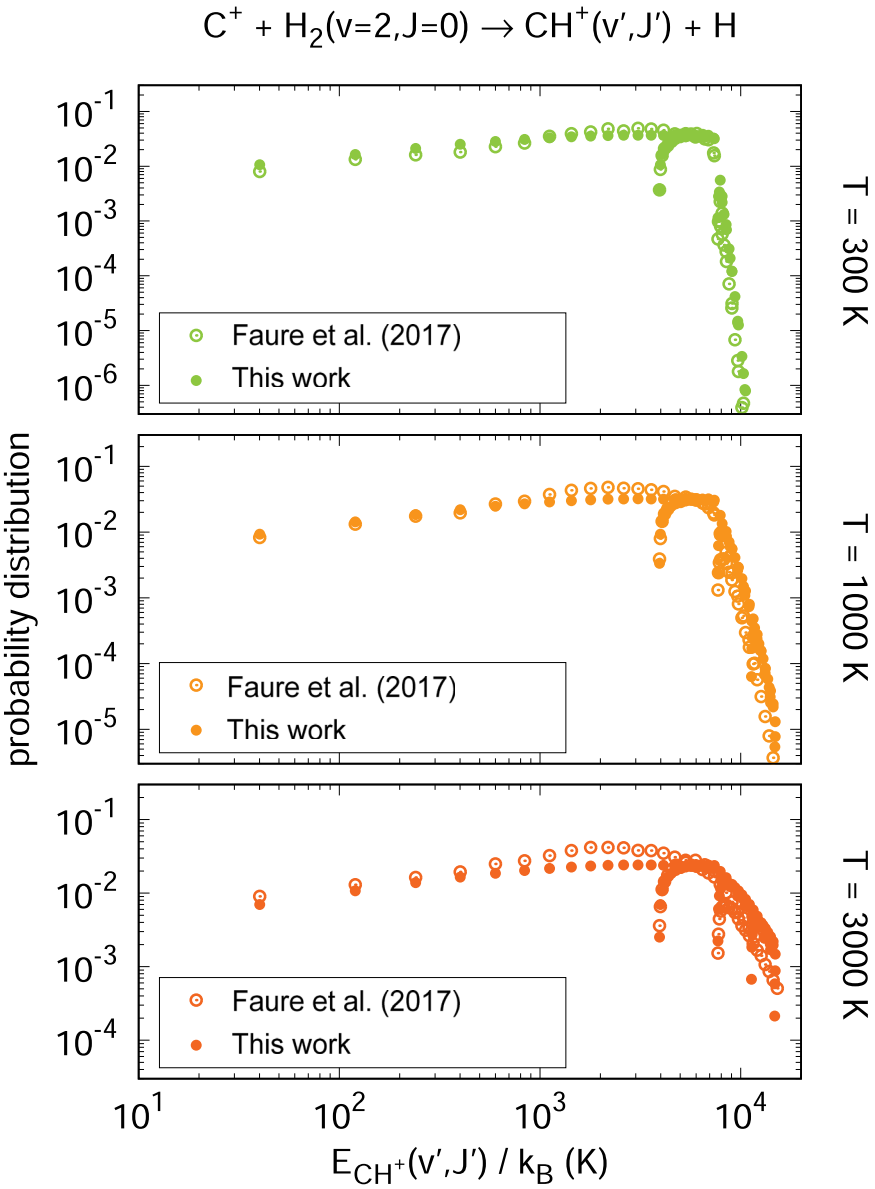

Figure 15. Probability distributions of forming CH^+ in its rovibrational levels (v', J') through the reaction of C^+ with $H_2(v = 2, J = 0)$ as a function of the level energy $E_{CH^+}(v', J')$. The distributions computed with Equation (B5) (filled circles) are compared with those obtained by F17 (open circles) for a kinetic temperature of 300 K (top panel), 1000 K (middle panel), and 3000 K (bottom panel).

the vibrational de-excitation rates of the $v = 1$, 2, 3 levels of CH^+ by collisions with e^- recently computed by Jiang et al. (2019).

An illustration of the prescription adopted for the CH^+-e^- collisional system is given in Figure 14. Although empirical, the above treatment has the advantage of limiting the collisional rates to the total de-excitation rate of pure rotational levels and providing simple and separated prescriptions of the dependences on ΔE, Δv, and ΔJ that favor elements of the collisional matrix close to the diagonal relative to those far from the diagonal, in fair agreement with the available data.

B.2. Reactive Collisional Excitation

Adopting the prescription of the Meudon PDR code, the total reaction rates of reaction 2 are first computed using the quasi-classical treatment of Herráez-Aguilar et al. (2014), who derived rate constants for 10 rovibrational levels of H_2 in $v = 0$ and $v = 1$. They are then scaled to reproduce the detailed time-dependent quantum calculations of Zanchet et al. (2013, hereafter Z13), who derived rate constants for the (v, J) = (0,0), (1, 0), and (1, 1) levels of H_2. The total reaction rates for all H_2 levels above (v, J) = (2,0) are set to the value obtained by Faure et al. (2017, hereafter F17) for that level.

The probability distribution of forming CH^+ in its rovibrational levels is deduced from the recent studies performed by Z13 and F17. For any level (v,J) of H_2, the probability $p(v', J')$ of forming CH^+ in a level (v', J') is assumed to scale as

$$p(v', J') \propto (2J' + 1)\exp(-0.08J') \text{ if } E < 0$$
$$\propto (2J' + 1)\exp(-0.08J')\exp(-E/k_BT) \text{ if } E \geq 0 \quad \text{(B5)}$$

where

$$E = E_0 + E_{CH^+}(v', J') - E_{H_2}(v, J) \quad \text{(B6)}$$

is the total energy balance for reaction 2, including the enthalpy E_0 of the reaction ($E_0/k_B = 4281$ K) and the energies $E_{CH^+}(v', J')$ and $E_{H_2}(v, J)$ of the (v', J') and (v,J) rovibrational levels of CH^+ and H_2, respectively.[15] Examples of the probability distributions obtained with Equation (B5) for $(v, J) = (2,0)$ are shown in Figure 15 and compared with the distributions calculated by F17. Although the above recipe appears to overestimate the production of CH^+ in highly excited states at high kinetic temperature, it provides a simple prescription that captures relatively well the strong dependences of the occupation probabilities on the total energy balance of reaction 2 and on the kinetic temperature.

ORCID iDs

David A. Neufeld https://orcid.org/0000-0001-8341-1646
P. Bryan Changala https://orcid.org/0000-0003-0304-9814
Alexandre Faure https://orcid.org/0000-0002-8270-9907
T. R. Geballe https://orcid.org/0000-0003-2824-3875
Karl M. Menten https://orcid.org/0000-0001-6459-0669
Helmut Wiesemeyer https://orcid.org/0000-0002-5135-8657

References

Agúndez, M., Goicoechea, J. R., Cernicharo, J., et al. 2010, ApJ, 713, 662
Beckwith, S., Neugebauer, G., Becklin, E. E., et al. 1980, AJ, 85, 886
Cernicharo, J., Liu, X.-W., González-Alfonso, E., et al. 1997, ApJL, 483, L65
Changala, B., Neufeld, D. A., & Godard, B. 2021, ApJ, 917, 16
Cho, Y.-S., & Le Roy, R. J. 2016, JChPh, 144, 024311
Cox, P., Huggins, P. J., Maillard, J.-P., et al. 2002, A&A, 384, 603
Cox, P., Maillard, J.-P., Huggins, P. J., et al. 1997, A&A, 321, 907
Cushing, M. C., Vacca, W. D., & Rayner, J. T. 2004, PASP, 116, 362
Doménech, J. L., Jusko, P., Schlemmer, S., et al. 2018, ApJ, 857, 61
Falgarone, E., Zwaan, M. A., Godard, B., et al. 2017, Natur, 548, 430
Faure, A., Halvick, P., Stoecklin, T., et al. 2017, MNRAS, 469, 612
Federman, S. R., Glassgold, A. E., & Kwan, J. 1979, ApJ, 227, 466
Ferland, G. J., Chatzikos, M., Guzmán, F., et al. 2017, RMxAA, 53, 385
Godard, B., & Cernicharo, J. 2013, A&A, 550, A8
Godard, B., Pineau des Forêts, G., Lesaffre, P., et al. 2019, A&A, 622, A100
Güsten, R., Wiesemeyer, H., Neufeld, D., et al. 2019, Natur, 568, 357
Hakalla, R., Kepa, R., Szajna, W., et al. 2006, EPJD, 38, 481
Hamilton, J. R., Faure, A., & Tennyson, J. 2016, MNRAS, 455, 3281
Hammami, K., Owono Owono, L. C., & Stäuber, P. 2009, A&A, 507, 1083
Hasegawa, T. I., & Kwok, S. 2001, ApJ, 562, 824
Herpin, F., Goicoechea, J. R., Pardo, J. R., et al. 2002, ApJ, 577, 961
Herráez-Aguilar, D., Jambrina, P. G., Menéndez, M., et al. 2014, PCCP, 16, 24800
Jiang, X., Yuen, C. H., Cortona, P., et al. 2019, PhRvA, 100, 062711
Latter, W. B., Dayal, A., Bieging, J. H., et al. 2000, ApJ, 539, 783
Lau, R. M., Werner, M., Sahai, R., & Ressler, M. E. 2016, ApJ, 833, 115
Lehmann, A., Godard, B., Pineau des Forêts, G., & Falgarone, E. 2020, A&A, 643, A101
Le Petit, F., Nehmé, C., Le Bourlot, J., et al. 2006, ApJS, 164, 506
Middlemass, D. 1990, MNRAS, 244, 294
Neufeld, D. A., Goto, M., Geballe, T. R., et al. 2020, ApJ, 894, 37
Plašil, R., Rednyk, S., Kovalenko, A., et al. 2021, ApJ, 910, 155
Rayner, J., Tokunaga, A., Jaffe, D., et al. 2016, Proc. SPIE, 9908, 990884
Roueff, E., Abgrall, H., Czachorowski, P., et al. 2019, A&A, 630, A58
Sauer, S. P. A., & Špirko, V. 2013, JChPh, 138, 024315
Smith, H. A., Larson, H. P., & Fink, U. 1981, ApJ, 244, 835
Sternberg, A., & Dalgarno, A. 1989, ApJ, 338, 197
Sternberg, A., & Neufeld, D. A. 1999, ApJ, 516, 371
Vacca, W. D., Cushing, M. C., & Rayner, J. T. 2003, PASP, 115, 389
Wesson, R., Cernicharo, J., Barlow, M. J., et al. 2010, A&A, 518, L144
Yu, S., Drouin, B., Pearson, J., et al. 2016, in 71st Int. Symp. on Molecular Spectroscopy, MH01 (Urbana, IL: ISMS), MH01
Zanchet, A., Godard, B., Bulut, N., et al. 2013, ApJ, 766, 80
Zhang, Y., Kwok, S. & Dinh-V-Trung 2008, ApJ, 678, 328
Zijlstra, A. A., van Hoof, P. A. M., & Perley, R. A. 2008, ApJ, 681, 1296

[15] In our treatment of reactive collisional excitation, we neglect any dependence of $p(v', J')$ on the rotational state, J, of the reactant H_2 molecule. To date, no quantum calculations are available for any case with $J > 1$; future calculations would be extremely desirable to determine the dependence on J, if any.